

**ACTIVE STEERING CONTROLLER DESIGN**

**M.Sc. Thesis by  
Sinan ÖNCÜ, Eng.**

**Department : Mechatronics Engineering**

**Programme: Mechatronics Engineering**

**NOVEMBER 2007**

**ACTIVE STEERING  
CONTROLLER DESIGN**

**M.Sc. Thesis by  
Sinan ÖNCÜ, Eng.  
518051017**

**Date of submission : 01 November 2007**

**Date of defence examination : 30 November 2007**

**Supervisor (Chairman) : Prof. Dr. Levent Güvenç**

**Members of the Examining Committee Asst.Prof. Tankut Acarman ( GÜ. )**

**Asst.Prof. Erdinç Altuğ ( İTÜ )**

**NOVEMBER 2007**

**İSTANBUL TEKNİK ÜNİVERSİTESİ ★ FEN BİLİMLERİ ENSTİTÜSÜ**

**AKTİF DİREKSİYON SİSTEMİ  
KONTROLCÜSÜ TASARIMI**

**YÜKSEK LİSANS TEZİ**

**Müh. Sinan ÖNCÜ  
518051017**

**Tezin Enstitüye Verildiği Tarih : 01 Kasım 2007**

**Tezin Savunulduğu Tarih : 30 Kasım 2007**

**Tez Danışmanı : Prof. Dr. Levent Güvenç**

**Diğer Jüri Üyeleri Yrd. Doç. Dr. Tankut Acarman ( GÜ. )**

**Yrd. Doç. Dr. Erdiñç Altuğ ( İTÜ )**

**KASIM 2007**

## **ACKNOWLEDGEMENT**

I would like to express my deep appreciation and thanks for my advisor Prof. Levent Güvenç who guided me at every stage of this study. I also acknowledge the support of the European Commission Framework Program 6 through project INCO-16426, support of Ford Otosan through project ÜG 03.016 and The Scientific and Technological Research Council of Turkey (TUBITAK). I have furthermore to thank Sertaç Karaman for his contributions in the theoretical studies and publications.

NOVEMBER 2007

Sinan ÖNCÜ

## TABLE OF CONTENTS

<b>ABBREVIATIONS.....</b>	<b>v</b>
<b>LIST OF TABLES.....</b>	<b>vi</b>
<b>LIST OF FIGURES.....</b>	<b>vii</b>
<b>LIST OF SYMBOLS.....</b>	<b>ix</b>
<b>SUMMARY.....</b>	<b>x</b>
<b>ÖZET.....</b>	<b>xi</b>
<b>1. INTRODUCTION.....</b>	<b>1</b>
1.1 Outline of the Thesis .....	1
<b>2. MATHEMATICAL BACKGROUND.....</b>	<b>3</b>
2.1 Parameter Space Approach.....	3
2.2 Controller Design in the Parameter Space.....	3
2.3 <i>D</i> - Stability .....	5
2.4 Mapping Frequency Domain Specifications into Parameter Space .....	8
<b>3. VEHICLE MODELS.....</b>	<b>10</b>
3.1 Vehicle Dynamics Modelling.....	10
3.1.1 Nonlinear single track model.....	10
3.1.2 Pacejka tire model.....	14
3.1.3 Simulink model of the nonlinear single track model.....	20
3.1.4 Linear single track model.....	26
3.2 Steering System Model .....	29
<b>4. EXPERIMENTAL SETUP.....</b>	<b>33</b>
4.1 Steering Test Tig.....	33
4.2 Experimental Vehicle.....	35
4.3 Active Steering System Hardware .....	36
<b>5. ELECTRIC POWER ASSISTED STEERING.....</b>	<b>41</b>
5.1 EPAS Controller Design .....	43
<b>6. STEER-BY-WIRE CONTROLLER DESIGN .....</b>	<b>44</b>
6.1 Disturbance Observer Based Steer-By-Wire Controller Design.....	46
6.1.1 Disturbance observer .....	46
6.1.2 <i>D</i> -Stable position controller design .....	50
<b>7. YAW STABILITY CONTROLLER DESIGN .....</b>	<b>52</b>
7.1 Disturbance Observer Based Steering For Yaw Stability Control.....	52
7.2 Multi-Objective Parameter Space Design.....	54

7.3 Simulation Studies .....	62
7.4 Hardware-in-The-Loop Test Setup .....	64
<b>8. FINAL CONCLUSION .....</b>	<b>67</b>
<b>REFERENCES .....</b>	<b>68</b>
<b>APPENDICES .....</b>	<b>70</b>
<b>VITA .....</b>	<b>74</b>

## **ABBREVIATIONS**

<b>ABS</b>	: Anti-lock Braking Sistem
<b>TCS</b>	: Traction Control Sistem
<b>RRB</b>	: Real Root Boundary
<b>IRB</b>	: Infinite Root Boundary
<b>CRB</b>	: Complex Root Boundary
<b>HPAS</b>	: Hydraulic Power Assisted Steering
<b>DC</b>	: Direct Current
<b>CAN</b>	: Controller Area Network
<b>EPAS</b>	: Electrical Power Assisted Steering
<b>HIL</b>	: Hardware-in-the-Loop
<b>DO</b>	: Disturbance Observer

## LIST OF TABLES

	<b>Page No</b>
<b>Table 3.1</b> Single Track Vehicle Model Parameters.....	11
<b>Tablo 3.2</b> Steering System Parameters.....	30



## LIST OF FIGURES

	Page No
<b>Figure 2.1</b> : <i>D</i> -Stable Regions.....	6
<b>Figure 2.2</b> : <i>D</i> -Stability Condition.....	7
<b>Figure 2.3</b> : Point Condition.....	9
<b>Figure 3.1</b> : Geometry of the single track vehicle model.....	10
<b>Figure 3.2</b> : Nonlinear and linearized single track model block diagrams	12
<b>Figure 3.3</b> : Tire forces acting on a single tire ...	14
<b>Figure 3.4</b> : Simulink block diagram used for simulating longitudinal forces.....	15
<b>Figure 3.5</b> : Longitudinal tire force vs slip ratio.....	16
<b>Figure 3.6</b> : Slip angle of a single tire.....	16
<b>Figure 3.7</b> : Simulink Block Diagram Used for Simulating Lateral Tire Forces.	17
<b>Figure 3.8</b> : Lateral Tire Force vs Slip Angle	18
<b>Figure 3.9</b> : Simulink Block Diagram Used for Simulating Self Aligning Moment	19
<b>Figure 3.10</b> : Self Aligning Moment vs Slip Angle	19
<b>Figure 3.11</b> : Simulink Model of the Non-Linear Single Track Model	20
<b>Figure 3.12</b> : Simulink Pacejka Tire Model	21
<b>Figure 3.13</b> : Tire-Chassis Projection Block	22
<b>Figure 3.14</b> : Simulink Implementation of the Vehicle Dynamics Equations	24
<b>Figure 3.15</b> : Simulink Implementation of the Kinematics Geometry Equations	25
<b>Figure 3.16</b> : Simple Driver Model	25
<b>Figure 3.17</b> : Linearized Single Track Model	26
<b>Figure 3.18</b> : Simulink Linear Tire Model	27
<b>Figure 3.19</b> : Linearized Tire/Chassis Projection Block	27
<b>Figure 3.20</b> : Simulink Implementation of the Linearized Vehicle Dynamics Block	28
<b>Figure 3.21</b> : Simulink Implementation of the Linearized Kinematics Block	29
<b>Figure 3.22</b> : Schematic Representation of the Double-pinion Steering System	29
<b>Figure 3.23</b> : Steering system block diagram	32
<b>Figure 4.1</b> : Steering Test Rig	33
<b>Figure 4.2</b> : Different steering architectures that can be investigated using the steering test rig	34
<b>Figure 4.3</b> : The Experimental Vehicle	36
<b>Figure 4.4</b> : The Electronic Control Unit Implemented on the Experimental Vehicle	37
<b>Figure 4.5</b> : Double Pinion Steering Rack Mechanism	38
<b>Figure 4.6</b> : DC Motor and Driver	38
<b>Figure 4.7</b> : Electrical Motor Connection on the Experimental Vehicle	39
<b>Figure 4.8</b> : Steering Wheel Angular Position Sensor	39
<b>Figure 4.9</b> : Instrumentation of the Torque Sensor	40
<b>Figure 4.10</b> : Yaw Rate Sensor	40

<b>Figure 5.1</b>	: EPAS Controller Structure	43
<b>Figure 5.2</b>	: Normalized Boost Curve	43
<b>Figure 6.1</b>	: Schematic representation of steer-by-wire system	44
<b>Figure 6.2</b>	: Schematic representation of steer-by-wire hardware-in-the-loop simulator components and their interactions	45
<b>Figure 6.3</b>	: Two loop control structure	46
<b>Figure 6.4</b>	: Disturbance Observer	47
<b>Figure 6.5</b>	: Model regulation performance of disturbance observer in high gain operating region	49
<b>Figure 6.6</b>	: Model regulation performance of disturbance observer in a highly nonlinear region	49
<b>Figure 6.7</b>	: region in the complex region	50
<b>Figure 6.8</b>	: $D$ -stable Solution Region	51
<b>Figure 6.9</b>	: Step response of the steer-by-wire controller	51
<b>Figure 7.1</b>	: Disturbance observer based yaw stability controller block diagram	53
<b>Figure 7.2</b>	: Region of uncertain parameters	54
<b>Figure 7.3</b>	: $D$ -stability region in the complex plane	55
<b>Figure 7.4</b>	: $D$ -stability regions for the six design points	56
<b>Figure 7.5</b>	: Overall $D$ -stability region	57
<b>Figure 7.6</b>	: Phase margin bounds and combined solution area for operating points	57
<b>Figure 7.7</b>	: Mixed sensitivity solution regions for the six design points	60
<b>Figure 7.8</b>	: Combined solution regions for the six design points	61
<b>Figure 7.9</b>	: Overall multi-objective solution region	61
<b>Figure 7.10</b>	: Step steering wheel inputs to uncontrolled and controlled models	62
<b>Figure 7.11</b>	: Step steering wheel inputs to uncontrolled and controlled models	63
<b>Figure 7.12</b>	: Stroboscopic plot	63
<b>Figure 7.13</b>	: Schematic representation of steer-by-wire hardware-in-the-loop simulator components and their interactions	64
<b>Figure 7.14</b>	: Step steering command input response simulation (normalized)	65
<b>Figure 7.15</b>	: Step yaw moment disturbance simulation (normalized)	66
<b>Figure 7.16</b>	: Commanded and actual steering actuator action	66
<b>Figure A.1</b>	: IO Characteristics of MicroAutobox	71
<b>Figure A.2</b>	: Technical Specifications of RapidPro SC Unit	72
<b>Figure A.3</b>	: Technical Specifications of RapidPro PU Unit	73

## LIST OF SYMBOLS

$F_f, F_r$	: Lateral wheel force at front (rear) wheel
$M_{zd}$	: Yaw disturbance moment
$r$	: Yaw rate
$\beta$	: Chassis side slip angle at vehicle center of gravity
$\alpha_f, \alpha_r$	: Front (rear) tire side slip angle
$v$	: Vehicle speed at center of gravity point
$l_f, l_r$	: Distance from front (rear) axle to center of gravity
$\delta_f$	: Front wheel steering angle
$m$	: The mass of the vehicle
$I_z$	: The moment of inertia w.r.t. a vertical axis through the center of gravity
$C_f, C_r$	: Front (rear) wheel cornering stiffness
$C_{f0}, C_{r0}$	: Nominal values of front (rear) wheel cornering stiffness
$\mu$	: Road friction coefficient
$R_e$	: Effective radius of the tire
$F_x, F_y$	: Total force acting in the x-axis / y-axis
$u$	: Side slip velocity
$J_c$	: Steering wheel & column moment of inertia
$K_c$	: Steering column torsional stiffness
$B_c$	: Steering column damping
$M_r$	: Rack mass
$B_r$	: Rack damping
$K_t$	: Tie or rack centering spring rate
$F_{tr}$	: Tie-rod force (road disturbance input)
$r_p$	: Pinion radius
$G$	: Gear ratio (motor)
$J_m$	: Motor moment of inertia
$K_m$	: Motor and gearbox torsional stiffness
$B_m$	: Motor and gearbox damping
$k$	: Motor torque and voltage constant
$L$	: Motor inductance
$T_d$	: Driver torque
$T_m$	: Motor torque
$x$	: Rack position
$\Theta_c$	: Column angular position
$\Theta_m$	: Motor angular position
$\tau_Q$	: Low pass filter time constant
$\tau_n$	: Nominal model time constant
$J_T$	: Total inertia of the steering system
$K_T$	: Total stiffness of the steering system
$B_T$	: Total damping of the steering system

## ACTIVE STEERING CONTROLLER DESIGN

### SUMMARY

This study is on the application of active steering and yaw stability control to a light commercial vehicle. First, models for vehicle dynamics and steering system were developed in Simulink. A linear single track model of the light commercial vehicle was used for controller design while its nonlinear version was used during hardware-in-the-loop simulations. Controller designs were tested using offline and hardware-in-the-loop simulations. A hardware-in-the-loop simulation test rig with the actual rack and pinion mechanism of the light commercial vehicle under study was built for this purpose. The hardware and geometry of the steering test rig are identical to the implementation of the steering system in the test vehicle. Unnecessary and expensive road testing is avoided with this approach as most problems are identified and solved in the hardware-in-the-loop simulation phase conducted in the laboratory where the steering subsystem and its controller exist as hardware and the rest of the vehicle being implemented exists as real time capable software. The first active steering controller designed was a boost curve type electric power assisted steering (EPAS) controller. The EPAS controller was implemented on a actual vehicle equipped with active steering system. In the next step, a steer-by-wire system was designed. Existing hardware-in-the-loop test rig used previously for electric power assisted steering studies was modified and changed into a steer-by-wire test rig. This setup was used for experimental verification of the steer-by-wire controller designed here. The third active steering controller was a steering based yaw stability controller. A multi-objective design method was used to map  $D$ -stability, mixed sensitivity and phase margin bounds into parameter space. The resulting controller was tested using offline and hardware-in-the-loop simulations.

## AKTİF DİREKSİYON SİSTEMİ KONTOLCÜSÜ TASARIMI

### ÖZET

Bu tezde bir hafif ticari araç için aktif direksiyon sistemi ve savrulma dinamiği kontrolcüsü tasarlanmış ve uygulanmıştır. İlk olarak, araç dinamiği ve direksiyon sistemleri Simulink kullanılarak bilgisayar ortamında modellenmiştir. Söz konusu hafif ticari araca ait parametreler kullanılarak oluşturulan doğrusal tek izli araç modeli kontrolcü tasarımında kullanılmıştır. Doğrusal olmayan tek izli araç modeli ise donanım içeren simülasyonlarda kullanılmıştır. Tasarlanan kontrolcüler çevrimdışı ve donanım içeren simülasyonlar gerçekleştirilerek sınanmıştır. Bu amaçla, gerçek araçtakine benzer bir direksiyon sistemi test amaçlı olarak laboratuvar ortamında kurulmuştur. Test düzeneğindeki direksiyon sistemi geometrisi ve donanımı test aracındaki ile aynıdır. Bu yaklaşım sayesinde gereksiz ve masraflı yol testlerine gerek kalmadan bir çok problem donanım içeren simülasyonlar aşamasında tespit edilerek giderilebilmektedir. Test düzeneğinde direksiyon sistemi donanım olarak mevcutken aracın geri kalanı gerçek zamanlı bir yazılım olarak uygulanmıştır. Tasarlanan aktif direksiyon sistemi kontrolcülerinden ilki elektrik güç takviyeli direksiyon sistemidir. Bu sistem, aktif direksiyon sistemi donanımlı bir test aracı üzerinde uygulanmıştır. Bir sonraki adımda sürücü ile tekerler arasındaki mekanik bağlantının tamamen devreden çıkarıldığı elektronik direksiyon sistemi tasarlanmıştır. Mevcut direksiyon test düzeneği bu amaçla değiştirilerek elektronik direksiyon sistemi kontrolcüsünün deneysel olarak sınanmasında kullanılmıştır. Tez kapsamında tasarlanan bir diğer kontrolcü de aktif direksiyon sistemi tabanlı bir savrulma kararlılığı kontrolcüsüdür. Bu kontrolcünün tasarımında  $D$ -kararlılık, karışık duyarlılık ve faz marjın sınırlamalarını sağlayan çok yönlü bir tasarım yöntemi parametre uzayında gerçekleştirilmiştir. Elde edilen kontrolcü çevrimdışı ve donanım içeren simülasyonlar gerçekleştirilerek test edilmiştir.

## **1. INTRODUCTION**

Safety of road transport is an important issue and has been the focus of a European Union white paper in 2001, where an ambitious target for road safety of achieving a 50% reduction of road fatalities by the year 2010 was set [1]. There are similar aims in the rest of the world as well. Improving the safety of road transport requires the development of road vehicle safety systems which fall into the three broad categories of passive, preventive/active and integrated safety systems. Seat belts, air bags and structural elements used to enhance crash safety are all passive safety devices. The aim in passive safety system design is to minimize the damage to the driver and the passengers of a road vehicle during an accident. On the contrary, the aim in preventive and active safety system design is to improve the response of the vehicle to driver inputs even in adverse situations and thereby avoid accidents. Preventive and active safety systems include well accepted systems like ABS (anti lock brakes), or TCS (traction control system) systems. Preventive and active safety systems are basically driving assistant systems with actuators. Preventive and active safety systems impart a temporary control authority transition from the driver to the underlying automatic control system in the case of dangerous situations like excessive yaw or roll motion that may eventually result in loss of control of the vehicle's dynamic behavior by the driver. Integrated safety systems are a new category of vehicle safety systems that fall between passive and active safety systems. In the case of integrated safety systems, the passive safety systems are prepared in advance to minimize injury risks to the vehicle inhabitants and pedestrians when the underlying automatic control system determines that the present preventive and active safety systems will not be able to avoid an accident. This may take the form of increasing the tension on seat belts, gripping the vehicle inhabitants with adaptable seats, preparing the airbags for faster deployment and using available automatic actuators to reduce the collision damage to pedestrians.

### **1.1 Outline of the Thesis**

The work in this thesis falls under the preventive and active safety systems category. The road vehicle under consideration is a light commercial vehicle, the Ford Transit Connect, developed and produced by Ford Otosan. The study has three main aims. The first aim is to improve the steering dynamics through an additional active

steering actuator. The second aim is to design a steer-by-wire system for the same vehicle. The third aim is to design a yaw stability controller.

In Chapter 2, the theoretical material used throughout the thesis study is explained. The parameter space method and its uses for controller design is presented. Parameter space techniques were used for both steer-by-wire controller design and yaw stability controller design. Later, the D-stability concept is presented and D-stable controller design in the parameter space is explained. The chapter ends with theoretical concepts on mapping frequency domain specifications into parameter space.

In Chapter 3, vehicle models developed for both simulation and controller design are presented. The nonlinear vehicle models were used for simulations and linear models were used for controller design. Vehicle dynamics and steering system dynamics equations are given in detail and their Simulink implementations are shown.

In Chapter 4, the experimental setups used to perform hardware-in-the-loop simulations are explained. Experimental setup used in this study consists of a steering test rig which was used for hardware-in-the-loop simulations and an experimental vehicle which was equipped with active steering hardware. The hardware components of the active steering system are explained in detail and their instrumentation on the experimental vehicle is shown.

In Chapters 5, 6 and 7 three active steering applications are explained which are:

- Electrical Power Assisted Steering
- Steer-By-Wire
- Steering Based Yaw Stability Controller Design

The thesis ends with final conclusions and discussions on the active steering concepts presented.

## 2. MATHEMATICAL BACKGROUND

### 2.1 Parameter Space Approach

Conventional methods for controller design like pole placement give unique controllers for each plant. No further robustness criteria can be incorporated in the design step [2]. The parameter space approach can be used to determine a set of coefficients for a given controller structure which simultaneously stabilizes a family of plants [3]. The parameter space approach allows to determine the set of parameters  $H$ , for which the characteristic polynomial  $p(s, h)$ ,  $h \in H$  is stable. The parameter vector may consist of uncertain plant parameters or it may consist of coefficients of a fixed structure controller.

Plotting the Hurwitz or  $D$ -stable regions into the parameter space is advantageous because of the ability of plotting several different specifications on top of each other. Parameter space approach also provides information about effects of parameter variations on stability and it provides information about the closeness to instability upon parameter variations. The resulting controllers are not fragile since they are chosen in the inner part of the parameter space.

### 2.2 Controller Design in the Parameter Space

In the center of the analysis that will be considered in this thesis lies two important theorems, one of them is the continuity of the roots and the other one is the boundary crossing theorem. The first theorem states that for an uncertain polynomial if the uncertain parameters change continuously then the locations of the roots of that polynomial will be traveling in complex plane in a continuous manner [3]. The latter theorem, named as the boundary crossing theorem can be stated as follows

The family of polynomials  $P(s, Q)$  is robustly stable, if and only if,

- i. there exists a stable polynomial  $p(s, q) \in P(s, Q)$ .
- ii.  $j\omega \notin \text{Roots}[P(s, Q)]$  for  $\forall \omega \geq 0$ .



So if one plots the curves to the parameter plane that  $j\omega \in \text{Roots}[P(s, Q)]$  holds, it becomes obvious that the parameters have to cross this boundary, for the roots of the characteristic polynomial to cross the imaginary axis. If all the roots of the polynomial were on the left half plane then basically this cross would destabilize the system. Thus this boundary can be named as the stability boundary.

In the synthesis however, the second condition will be used in a different manner. Noting that if the value of the polynomial has zero value for  $\exists \omega \geq 0$  then it is basically has a root on the imaginary axis exactly at that frequency. If,

$$p(j\omega, q) = 0 \quad (2.1)$$

holds for some  $q \in Q$  then this polynomial family is on the stability margin. The task in the controller design is to plot the  $q$  values on the parameter space such that (2.1) holds. In this manner the stability boundaries can be observed upon variations of  $q \in Q$ .

Choosing two parameters to be varying and evaluating (2.1) would yield,

$$\begin{aligned} p(j\omega, q) &= (a_0(q) - a_2(q)\omega^2 + a_4(q)\omega^4 - \dots) \\ &+ j\omega(a_1(q) - a_3(q)\omega^2 + a_5(q)\omega^4 - \dots) = 0 \end{aligned} \quad (2.2)$$

Equation (2.2) can be broken up into two separate equations,

$$\begin{aligned} a_0(q) - a_2(q)\omega^2 + a_4(q)\omega^4 - \dots &= 0 \\ a_1(q) - a_3(q)\omega^2 + a_5(q)\omega^4 - \dots &= 0 \end{aligned} \quad (2.3)$$

Now, let us fix all the uncertain parameters except two, which may be uncertain parameters of the plant or the controller,

$$a_0(q_1, q_2) - a_2(q_1, q_2)\omega^2 + a_4(q_1, q_2)\omega^4 - \dots = 0 \quad (2.4)$$

$$\omega(a_1(q_1, q_2) - a_3(q_1, q_2)\omega^2 + a_5(q_1, q_2)\omega^4 - \dots) = 0 \quad (2.5)$$

A first approach should be to eliminate  $\omega$  from the above equations and then plot the solution into the  $q_1, q_2$  plane. But note that this would then plot the solutions for complex values of  $\omega$  [3]. So instead of elimination of  $\omega$ , it is chosen as a parameter

and evaluated in the interval  $0 \leq \omega \leq \infty$ . After each evaluation the parameters  $q_1, q_2$  are solved from the equation set (2.4), and the result is plotted in the parameter space. If the grid over the frequency  $\omega$  is dense enough, then the resulting curve will be a candidate for the stability boundary. By leaving  $\omega$  in the equations one can restrict its values to non-negative real values, avoiding some fictitious boundaries, that  $\omega$  takes complex values.

Roots of the uncertain polynomial can be crossing the imaginary axis through  $\omega = 0$ ,  $\omega = \infty$  or  $0 < \omega < \infty$ . Note that for  $\omega = 0$  equation (2.5) drops and the two parameters in consideration become dependent. Then the solution becomes single line in the parameter space. The equation of this line can be obtained from (2.4) explicitly. This line provides the boundary that a crossing occurs from the origin, and is called the “real root boundary” (RRB). This condition is equivalent to  $a_0 = 0$ . The crossing over from  $\omega = \infty$  is possible when the polynomial drops degree, which can be given as  $a_n = 0$ . The equation is again explicit in terms of the uncertain parameters, and it forms a line in the two dimensional parameter space. This line is called the “infinite root boundary” (IRB). Finally the solution of (2.4) and (2.5) for  $0 < \omega < \infty$  gives curves in the two dimensional parameter space and these curves are called the “complex root boundary” (CRB).

### 2.3 *D- Stability*

The Hurwitz stability gives the stable regions in the parameter space, however, it does not provide any idea about the eigenvalue specifications. To achieve defined performance requirements the closed loop eigenvalues must be located at a specified region which is called *D*-stable region. To make pole region specifications is more natural for the designer, because generally we don't know exact positions of the desired closed loop poles, but we have an idea about desired region. This method allows to consider specifications like settling time, damping and bandwidth. Corresponding root locations are shown in Figure 2.1.

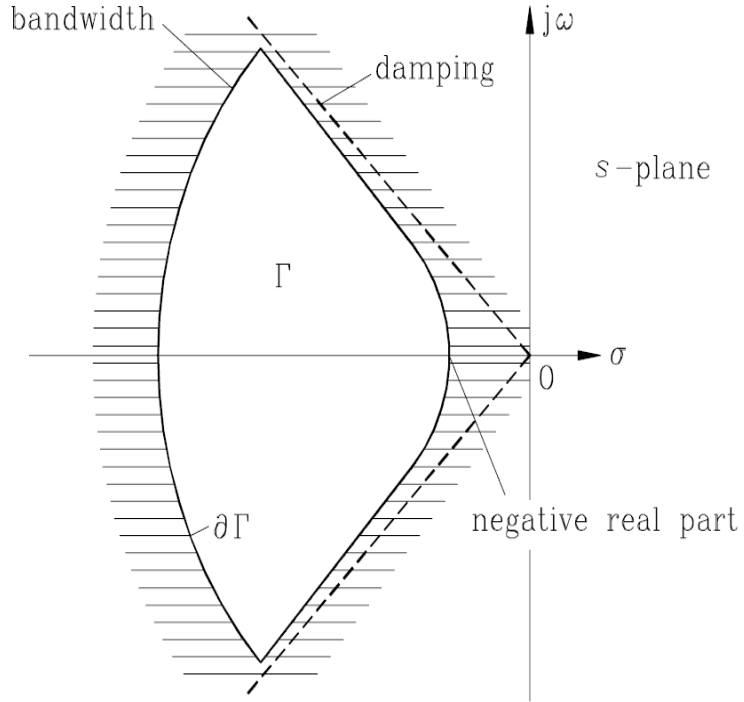


**Figure 2.1:** *D*-stable regions [4]

To make pole region specifications is more natural for the designer, because generally we don't know exact positions of the desired closed loop poles, but we have an idea about desired region [5].

The *D*-stability boundary ( $\partial\Gamma$ ) can be described mathematically by:

$$\partial\Gamma = \{s | s = \sigma(a) + j\omega(a), a \in [a^-, a^+]\} \quad (2.6)$$

Now, the *D*-stability boundary has to be mapped to the parameter space to obtain  $\mathcal{Q}_{\Gamma\text{-stable}}$ . For this task, we need to express  $\partial\Gamma$  in a more convenient way. For the *D*-stable region shown in Figure 2.2 the *D*-stability boundary can be expressed as

$$\partial\Gamma = \partial\Gamma_1 + \partial\Gamma_2 + \partial\Gamma_3 \quad (2.7)$$

Each of these boundaries define a parameter mentioned above.

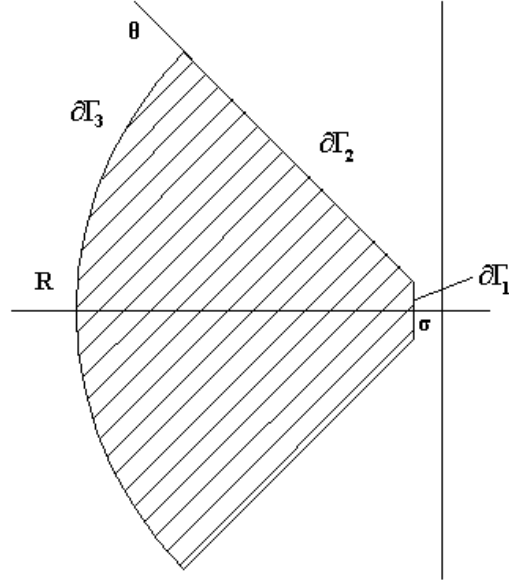


**Figure 2.2:** *D*-stability condition

$\sigma$  defines the minimum real part when the root is close to origin, and the angle  $\theta$  here defines a minimum damping value, finally the  $R$  value defines a maximum absolute value for the roots. To map the boundary of the gamma region given in Figure 2.2 the following can be substituted in to the equations (2.4) and (2.5),

For boundary  $\partial\Gamma_1$ ,

$$s = \sigma + j\omega \quad (2.8)$$

can be used, and  $\omega$  can be gridded between necessary values to obtain the boundary.

Similarly for boundary  $\partial\Gamma_2$ ,

$$s = re^{j\theta} \quad (2.9)$$

can be used, and this time  $r$  can be gridded between necessary values to obtain the corresponding boundary.

Finally for  $\partial\Gamma_3$

$$s = Re^{j\theta} \quad (2.10)$$

can be substituted, and  $\theta$  can be gridded to obtain the boundary in parameter space. When making such substitutions real root boundaries must also be taken into account.

## 2.4 Mapping Frequency Domain Specifications into Parameter Space

The aim of this section is to map the frequency domain criteria of robust control to parameter space. The mixed sensitivity problem will be considered in the analysis. In the parameter space the regions where the following specification,

$$|W_s S| + |W_t T| < 1 \quad \text{for} \quad \forall \omega \quad (2.11)$$

Defining the condition for search of a boundary such that

$$|W_s S| + |W_t T| = 1 \quad (2.12)$$

The above condition is named as the point condition and it illustrates the condition that the robust performance plot touches the robust performance margin. This condition can be restated as follows

$$|W_s| + |W_t L| = |1 + L| \quad \text{for} \quad \forall \omega \quad (2.13)$$

Then using the cosine rule as shown in figure 1,

$$|L| = \frac{-\cos \theta_L + |W_s| |W_t| \pm \sqrt{Disc}}{1 - |W_t|^2} \quad (2.14)$$

where

$$Disc = 1 + \cos^2 \theta_L - 2 |W_s| |W_t| \cos \theta_L + |W_s|^2 + |W_t|^2 \quad (2.15)$$

can be stated.

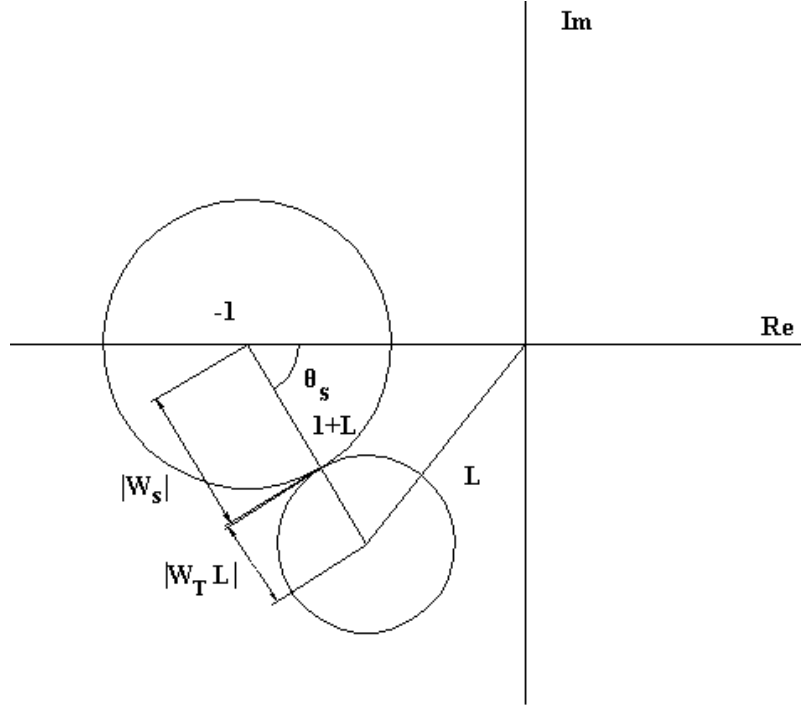


**Figure 2.3:** The point condition

Then the loop gain is solved from (2.14), which is dependent only to the weighted sensitivities. The solution must be made by gridding  $\theta_L$  and  $\omega$ . Then the controller parameters can be found by,

$$L = KG = (K_R + jK_I)G \quad (2.16)$$

where  $G$  is the plant dynamics and is known and  $L$  is the loop gain obtained from the solution of equation (2.14).  $K$  is a fictitious compensator and can be used to represent either controller parameters or uncertain parameters.

### 3. VEHICLE MODELS

#### 3.1 Vehicle Dynamics Modelling

##### 3.1.1 Nonlinear Single Track Model

The nonlinear single track model, also called the bicycle model is shown in Figure 3.1. The single track vehicle model captures the lateral dynamics of a road vehicle quite accurately in handling maneuvers where lateral acceleration does not exceed 0.3g.

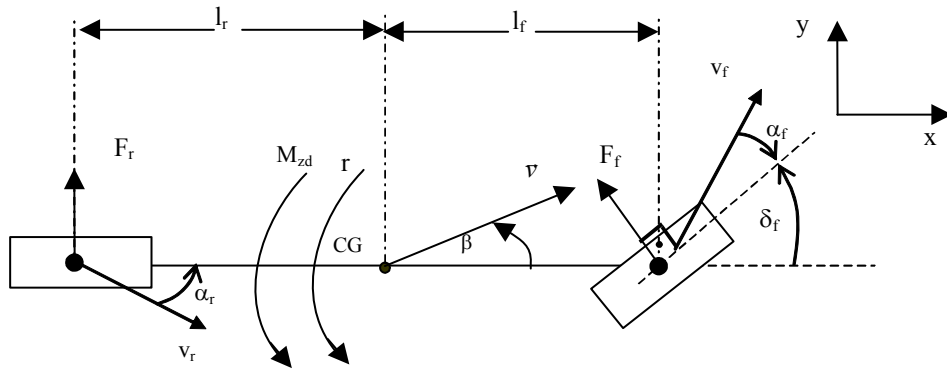


**Figure 3.1:** Geometry of the single track vehicle model

The nomenclature used in defining the major variables and geometric parameters of the single track are given in Table 3.1.

The nonlinear single track model is characterized by the force coordinate transformation due to steering angle projection given by [6]:

$$\begin{bmatrix} \sum F_x \\ \sum F_y \\ \sum M_z \end{bmatrix} = \begin{bmatrix} -\sin \delta_f & -\sin \delta_r \\ \cos \delta_f & \cos \delta_r \\ l_f \cos \delta_f & -l_r \cos \delta_r \end{bmatrix} \begin{bmatrix} F_f \\ F_r \end{bmatrix} \quad (3.1)$$

**Table 3.1:** Single Track Vehicle Model Parameters

Symbol	Explanation
$F_f (F_r)$	Lateral wheel force at front (rear) wheel
$M_{zd}$	Yaw disturbance moment
$r$	Yaw rate
$\beta$	Chassis side slip angle at vehicle center of gravity
$\alpha_f (\alpha_r)$	Front (rear) tire side slip angle
$v$	Vehicle speed at center of gravity point
$l_f (l_r)$	Distance from front (rear) axle to center of gravity
$\delta_f$	Front wheel steering angle
$m$	The mass of the vehicle
$I_z$	The moment of inertia w.r.t. a vertical axis through the center of gravity
$c_f (c_r)$	Front (rear) wheel cornering stiffness
$\mu$	Road friction coefficient

the dynamics equations

$$\begin{bmatrix} mv(\dot{\beta} + r) \\ m\dot{v} \\ I_z \dot{r} \end{bmatrix} = \begin{bmatrix} -\sin \beta & \cos \beta & 0 \\ \cos \beta & \sin \beta & 0 \\ 0 & 0 & 1 \end{bmatrix} \begin{bmatrix} \sum F_x \\ \sum F_y \\ \sum M_z \end{bmatrix} \quad (3.2)$$

and the equations of kinematics/geometry



$$\tan \beta_f = \tan \beta + \frac{l_f r}{v \cos \beta} \quad (3.3)$$

$$\tan \beta_r = \tan \beta - \frac{l_r r}{v \cos \beta} \quad (3.4)$$

The tire longitudinal forces  $F_f$  and  $F_r$  are nonlinear functions of the corresponding side slip angles  $\alpha_f$  and  $\alpha_r$ .  $F_f$  and  $F_r$  also depend on the friction characteristics between the road and the tires. The nonlinear single track model is illustrated in the top part of the block diagram of Figure 3.2 while its linearized version is shown in the bottom part of the same figure.

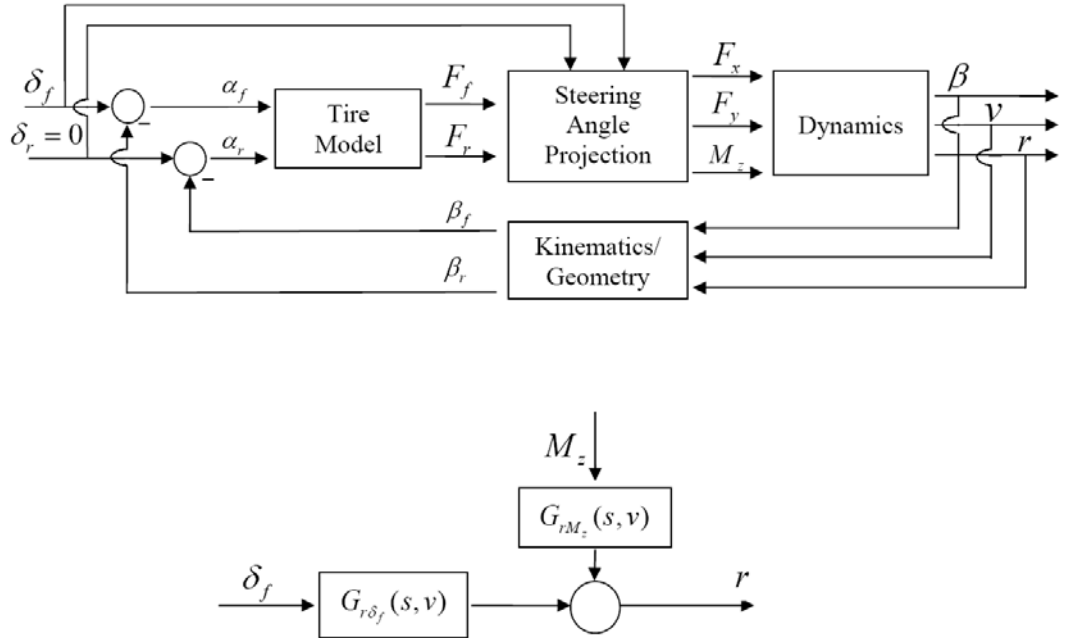


**Figure 3.2:** Nonlinear (top) and linearized (bottom) single track model block diagrams

The nonlinear single track model is linearized assuming small steering angles  $\delta_f$  and small side slip angle  $\beta$ . The tire force characteristics are linearized as

$$F_f(\alpha_f) = \mu C_{f0} \alpha_f = C_f \alpha_f, \quad F_r(\alpha_r) = \mu C_{r0} \alpha_r = C_r \alpha_r \quad (3.5)$$

with the tire cornering stiffnesses  $C_f$ ,  $C_r$  the road-tire friction coefficient  $\mu$  and the tire side slip angles given by

$$\alpha_f = \delta_f - \left( \beta + \frac{l_f}{v} r \right) \quad (3.6)$$

$$\alpha_r = - \left( \beta - \frac{l_r}{v} r \right) \quad (3.7)$$

Note that  $C_{f0}$  and  $C_{r0}$  in (5) are the nominal values for dry road ( $\mu = \mu_n = 1$ ) of the tire cornering stiffnesses. The transfer function from the front wheel steering angle  $\delta_f$  to the yaw rate  $r$  is given by :

$$G_{r\delta_f}(s, v) = \frac{r(s)}{\delta_f(s)} = \frac{b_1(v)s + b_0(v)}{a_2(v)s^2 + a_1(v)s + a_0(v)} \quad (3.8)$$

with

$$\begin{aligned} b_0 &= c_f c_r (l_f + l_r) v \\ b_1 &= c_f l_f m v^2 \\ a_0 &= c_f c_r (l_f + l_r)^2 + (c_r l_r - c_f l_f) m v^2 \\ a_1 &= (c_f (I_z + l_f^2 m) + c_r (I_z + l_r^2 m)) v \\ a_2 &= I_z m v^2 \end{aligned} \quad (3.9)$$

$G_{r\delta_f}(s, v)$  in (3.8) is also called the steering wheel input response transfer function here. The d.c. gain of the nominal single track model (3.8) is

$$K_n(v) = \lim_{s \rightarrow 0} G_{r\delta_f}(s, v) \Big|_{\mu=\mu_n=1} \quad (3.10)$$

at the chosen longitudinal speed  $v$  and for  $\mu = \mu_n = 1$ .

### 3.1.2 Pacejka Tire Model

The Pacejka tire model provides a method for calculating longitudinal, lateral tire forces and aligning moment for a wide range of operating conditions [7]. This model is also called Magic Tire Formula since it is based on experimental data and not on analytical formulas.

#### Longitudinal Tire Forces

Tire forces acting on a single tire during traction are shown in Figure 3.3.



**Figure 3.3:** Tire Forces Acting on a Single Tire [8]

Slip is defined as the amount of sliding at the road interface and is calculated using the following formulas :

$$s = (wR_e - V_x) / V_x \quad (3.11)$$

for braking and

$$s = (wR_e - V_x) / wR_e \quad (3.12)$$

for traction.

Longitudinal force acting on a tire is a function of slip ratio. In the Pacejka tire model these forces are calculated using empirical tire datas and the following formulas:

$$F_x(s) = D \sin[C \arctan(B(s + Sh) - E(B(s + Sh)))] + S_v \quad (3.13)$$

where

$$\begin{aligned} C &= b_0 \\ D &= \mu_p Fz \\ \mu_p &= b_1 Fz + b_2 \\ BCD &= (b_3 Fz^2 + b_4 Fz) e^{-b_5 Fz} \\ E &= b_6 Fz^2 + b_7 Fz + b_8 \end{aligned} \quad (3.14)$$

The relevant Pacejka tire parameters are obtained from [9]. In Figure 3.4 Simulink block diagram used to simulate longitudinal forces acting on the selected tire is shown.

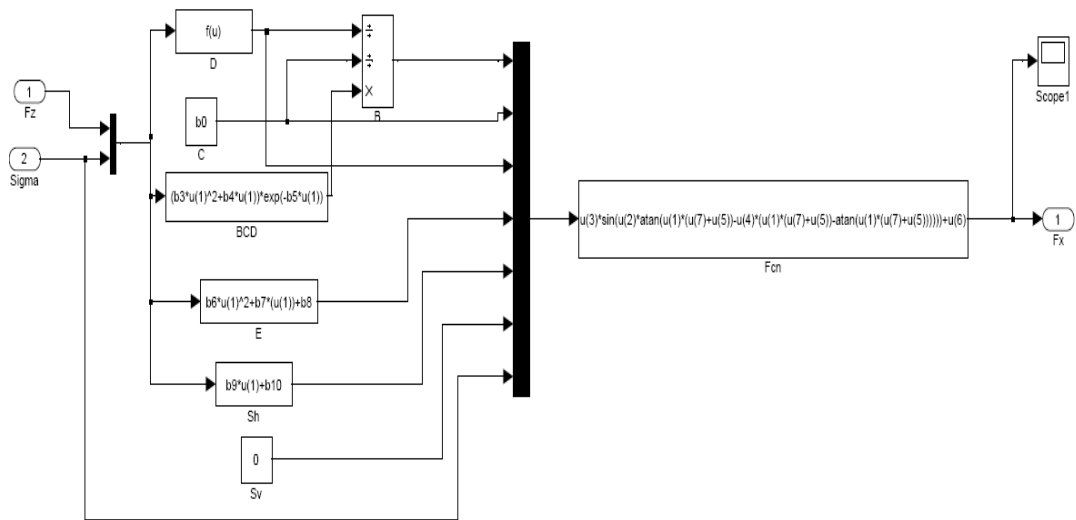
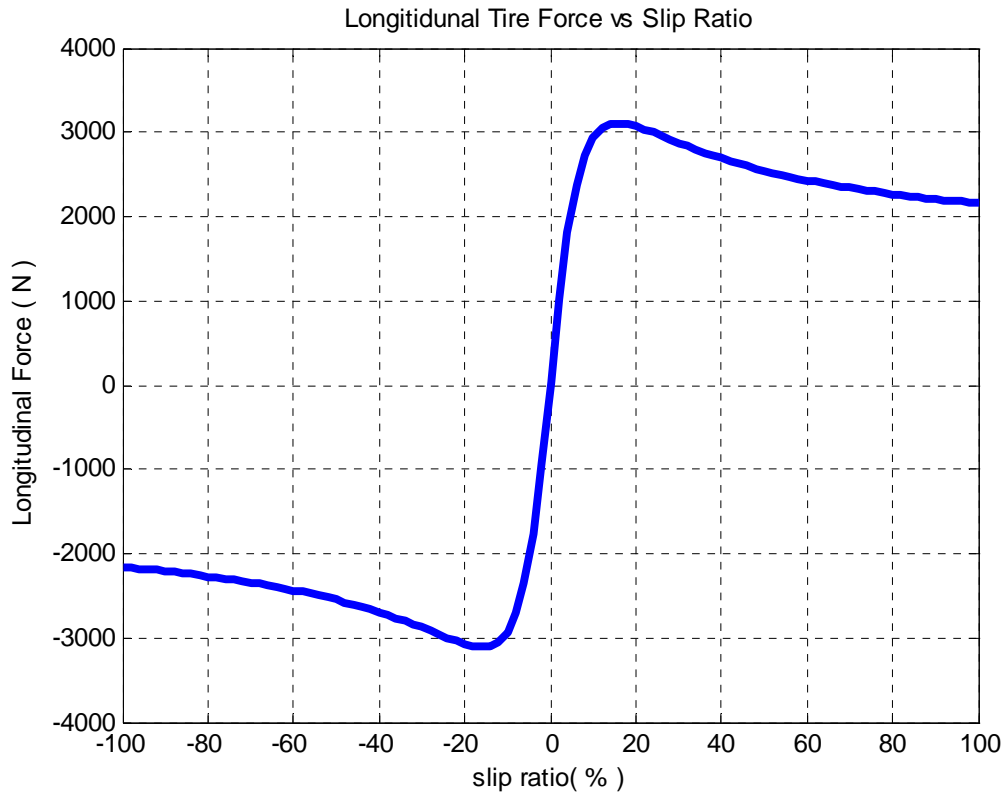


Figure 3.4. Simulink Block Diagram Used for Simulating Longitudinal Forces

The simulation results are shown in Figure 3.5.



**Figure 3.5:** Longitudinal Tire Force vs Slip Ratio

### Lateral Tire Forces

Slip angle shown in Figure 3.6. is defined as the angle between a rolling wheel's actual direction of travel and the direction towards which it is pointing ( the angle of the vector sum of wheel translational velocity  $v$  and side slip velocity  $u$ ). This slip angle results in a force perpendicular to the wheel's direction of travel.

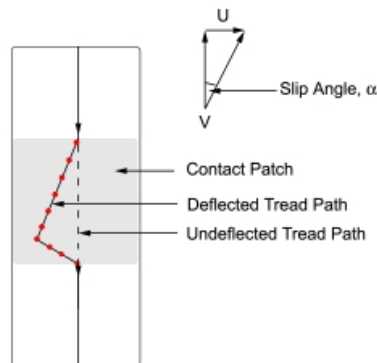


**Figure 3.6:** Slip Angle of a Single Tire [8]

This force is the lateral tire force. In the Pacejka model these forces are calculated using empirical tire datas and the following formula:

$$F_y(s) = D \sin[C \arctan(B(\alpha + Sh) - E(B(\alpha + Sh))))] + S_v \quad (3.15)$$

where

$$C = a_0$$

$$D = \mu_{yp} F_z$$

$$\mu_p = a_1 F_z + a_2$$

$$BCD = a_3 \sin[2 \arctan(\frac{F_z}{a_4})](1 - a_5 |\gamma|) \quad (3.16)$$

$$E = a_6 F_z + a_7$$

$$S_h = a_8 \gamma + a_9 F_z + a_{10}$$

$$S_v = a_{11} \gamma F_z + a_{12} F_z + a_{13}$$

A set of Pacejka tire parameters can be found in the literature. In this thesis paramaters in [9] were used. In Figure 3.7 Simulink block diagram used to simulate lateral forces acting on the selected tire is shown.

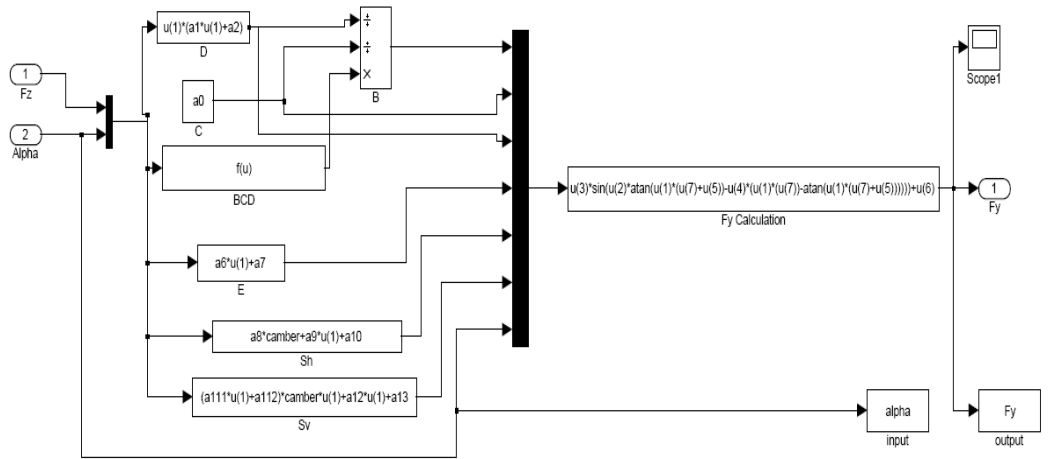


**Figure 3.7:** Simulink Block Diagram Used for Simulating Lateral Tire Forces

The simulation results are shown in Figure 3.8.

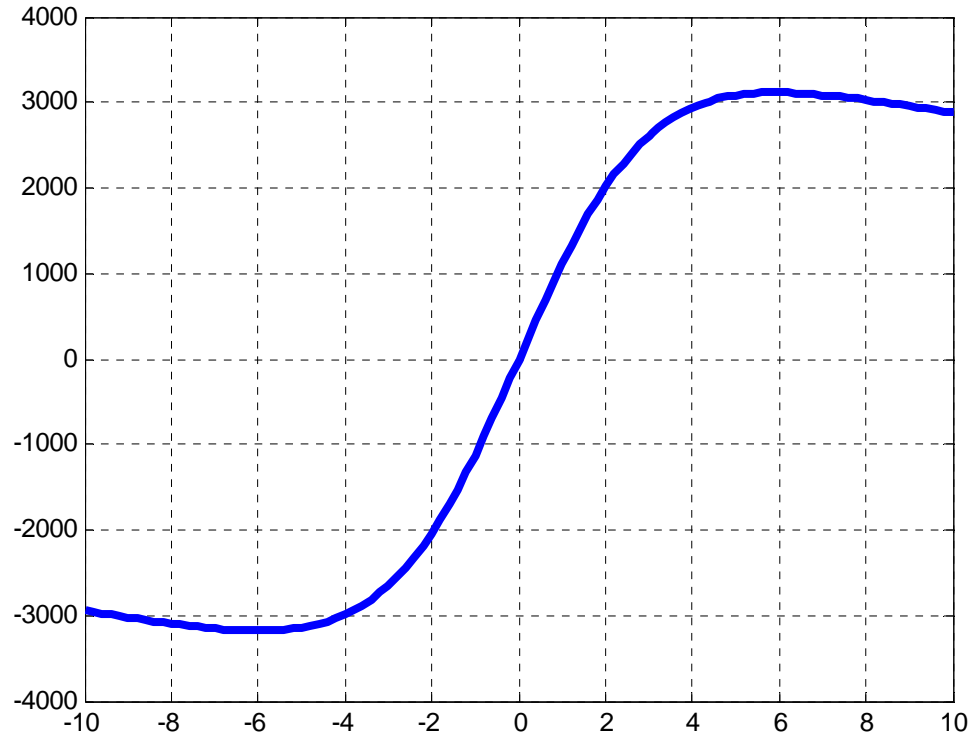


**Figure 3.8:** Lateral Tire Force vs Slip Angle

#### **Self- Aligning Moment:**

The pneumatic trail is the moment arm through which the lateral force acts. The fact that lateral force acts behind the centerline results in self aligning moment.

In the Pacejka model these forces are calculated using empirical tire datas and the following formulas:

$$M_{sa}(s) = D \sin[C \arctan(B\alpha - E(B(\alpha)))] \quad (3.17)$$

where:

$$\begin{aligned} C &= c_0 \\ D &= c_1 Fz^2 + c_2 Fz \\ E &= (c_7 Fz^2 + c_8 Fz + c_9)(1 - c_{10} |\gamma|) \\ BCD &= (c_3 Fz^2 + c_4 Fz)(1 - c_6 |\gamma|) e^{-c_5 Fz} \\ S_h &= c_{11} \gamma + c_{12} Fz + c_{13} \\ S_v &= (c_{14} Fz^2 + c_{15} Fz) \gamma + c_{16} Fz + c_{17} \end{aligned} \quad (3.18)$$

Pacejka tire parameters for self-aligning force calculations are from [9]. In the Figure 3.9 Simulink block diagram used to simulate self-aligning forces acting on the selected tire is shown.

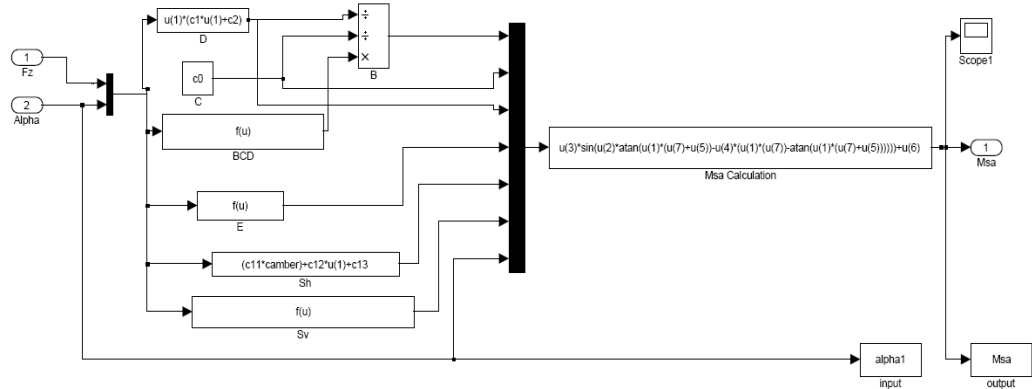


**Figure 3.9:** Simulink Block Diagram Used for Simulating Self Aligning Moment

The simulation results are shown in Figure 3.10.

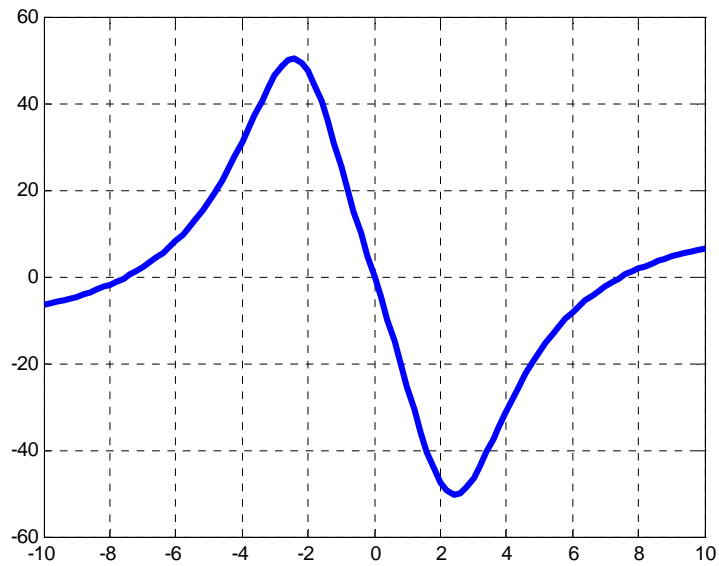


**Figure 3.10:** Self Aligning Moment vs Slip Angle



### 3.1.3 Simulink Model of the Nonlinear Single Track Model

The non-linear single track model shown in Figure 3.11 consists of the following subsystems:

- i. Tire Model
- ii. Tire Chassis Projection
- iii. Vehicle Dynamics
- iv. Kinematics – Geometry
- v. Simple Driver Model

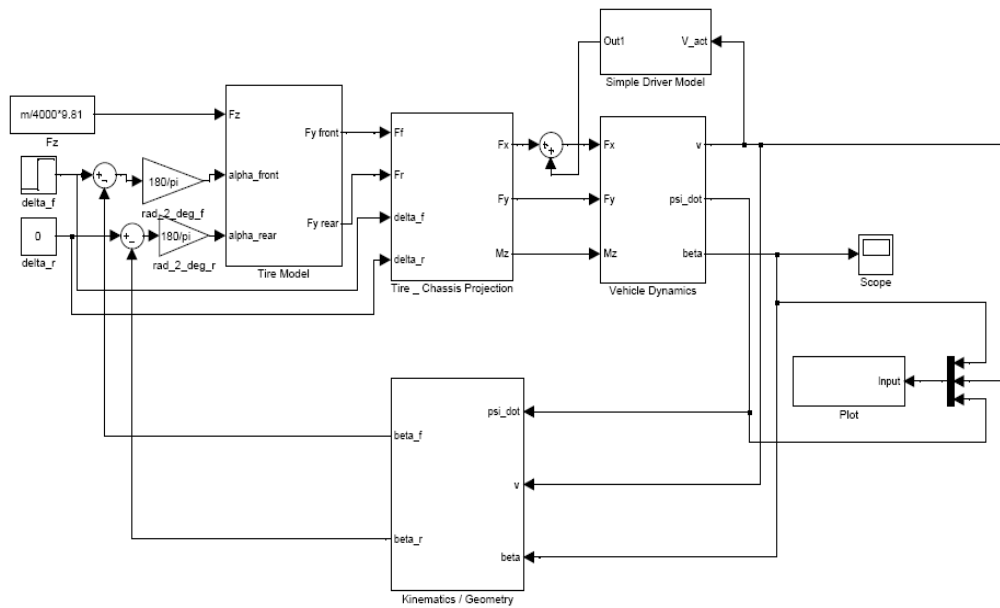


**Figure 3.11:** Simulink Model of the Non-Linear Single Track Model

Each of these sub-systems will be explained in the following sections.

### Simulink Pacejka Tire Model

In this sub-system the forces between the road surface and the wheels are modelled. Pacejka tire model is used to calculate lateral tire forces. The model is shown in Figure 3.12.

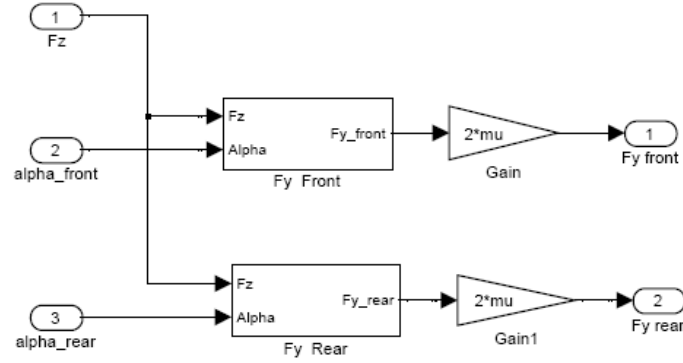


**Figure 3.12:** Simulink Pacejka Tire Model

Inputs to this block are:

- i.  $\alpha_f = \delta_f - \beta_f$  : Front tire side slip angle (deg)
- ii.  $\alpha_r = \delta_r - \beta_r$  : Rear tire side slip angle (deg)
- iii.  $F_z = mg/4000$ : weight distribution on a single tire

Outputs of this block are:

- i. Fy front: Lateral forces formed by the front tire pairs of the vehicle in the tire coordinate axis
- ii. Fy rear : Lateral forces formed by the rear tire pairs of the vehicle in the tire coordinate axis

Within the tire model block outputs of front and rear tire models are multiplied by two so that the total force exerted by lumped tire pairs ( left and right ) are obtained as shown in Figure 3.12. There is also another gain factor  $\mu$  ( $\mu$ ) that represents the road friction coefficient which is taken as unity gain for dry road.

### Tire - Chassis Projection

It was previously stated that the tire forces were obtained in the tire coordinate axis. In the Tire-Chassis Projection Block, effects of these forces on the vehicle chassis

are calculated by using trigonometric identities. The Tire-Chassis Projection Block shown in Figure 3.13 has the following input ports:

- i. Ff: Front lateral force in the tire coordinate axis
- ii. Fr: Rear lateral force in the tire coordinate axis
- iii. delta\_f : front tire steering angle
- iv. delta\_r: rear tire steering angle

And the output ports of the block are:

- i. Fx: the sum of forces in the x-axis.
- ii. Fy: the sum of forces in the y-axis
- iii. Mz: the sum of moments around the z axis.

The relations between input and output were given in (3.1). The implementation of these equations in Simulink are shown in Figure 3.13.

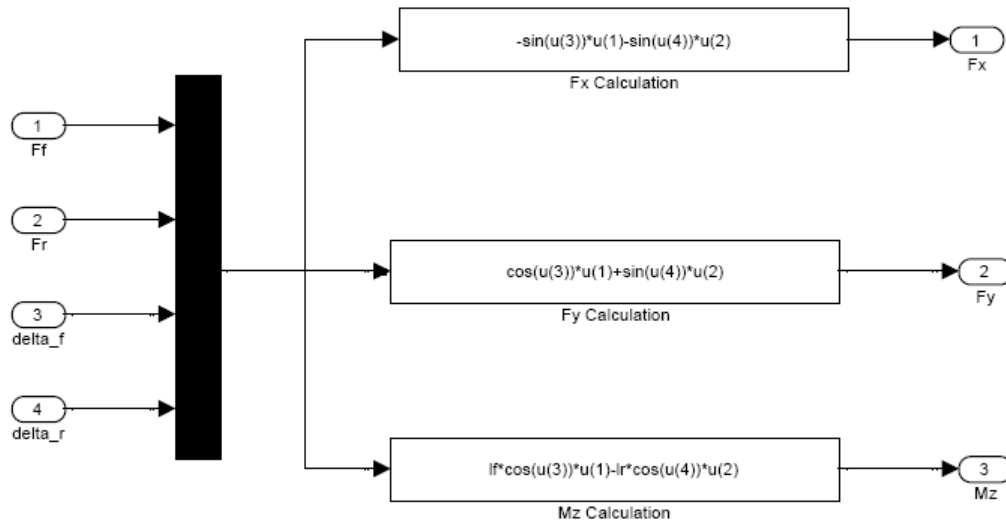


**Figure 3.13: Tire-Chassis Projection Block**

### Vehicle Dynamics Block

Now that total forces and moments acting on the vehicle body are obtained these values can be used to solve vehicle dynamics equations. The velocity and acceleration of the c.o.g. of the vehicle can be expressed by

$$\vec{V} = V.\cos\beta.\vec{i} + V.\sin\beta.\vec{j} \quad (3.19)$$

And

$$\vec{a} = \frac{d\vec{v}}{dt} = \left[ \dot{V} \cos \beta - V (\sin \beta) \dot{\beta} \right] \vec{i} + \left[ \dot{V} \sin \beta + V (\cos \beta) \dot{\beta} \right] \vec{j} + V \cos \beta \frac{d\vec{i}}{dt} + V \sin \beta \frac{d\vec{j}}{dt} \quad (3.20)$$

where

$$\frac{d\vec{i}}{dt} = \dot{\psi} \vec{k} \times \vec{i} = \dot{\psi} \vec{j} \quad (3.21)$$

$$\frac{d\vec{j}}{dt} = \dot{\psi} \vec{k} \times \vec{j} = -\dot{\psi} \vec{i} \quad (3.22)$$

The acceleration equation can now be written as:

$$\vec{a} = \frac{d\vec{v}}{dt} = \left[ \dot{V} \cos \beta - V (\sin \beta) \dot{\beta} \right] \vec{i} + V \cos \beta \dot{\psi} \vec{j} + \left[ \dot{V} \sin \beta + V (\cos \beta) \dot{\beta} \right] \vec{j} - V \sin \beta \dot{\psi} \vec{i} \quad (3.23)$$

Collecting the likely terms:

$$\begin{aligned} \vec{a} = \frac{d\vec{v}}{dt} &= \left[ \dot{V} \cos \beta - V (\sin \beta) \dot{\beta} - V \sin \beta \dot{\psi} \right] \vec{i} + \left[ \dot{V} \sin \beta + V (\cos \beta) \dot{\beta} + V \cos \beta \dot{\psi} \right] \vec{j} \\ &= \left[ \dot{V} \cos \beta - V (\dot{\beta} + \dot{\psi}) \sin \beta \right] \vec{i} + \left[ \dot{V} \sin \beta + V (\dot{\beta} + \dot{\psi}) \cos \beta \right] \vec{j} \\ &= a_x \vec{i} + a_y \vec{j} \end{aligned} \quad (3.24)$$

By using Newton's second law:

$$\begin{aligned} \sum F_x; \quad m a_x &= F_x \quad \rightarrow \quad m \left[ \dot{V} \cos \beta - V (\dot{\beta} + \dot{\psi}) \sin \beta \right] = F_x \\ \sum F_y; \quad m a_y &= F_y \quad \rightarrow \quad m \left[ \dot{V} \sin \beta + V (\dot{\beta} + \dot{\psi}) \cos \beta \right] = F_y \\ \sum M_z; \quad I_z \ddot{\psi} &= M_z \end{aligned} \quad (3.25)$$

Putting these equations into the matrix form gives:

$$\begin{bmatrix} -\sin \beta & \cos \beta & 0 \\ \cos \beta & \sin \beta & 0 \\ 0 & 0 & 1 \end{bmatrix} \cdot \begin{bmatrix} m v (\dot{\beta} + r) \\ m \dot{v} \\ J \dot{r} \end{bmatrix} = \begin{bmatrix} F_x \\ F_y \\ M_z \end{bmatrix} \quad (3.26)$$

$$\begin{bmatrix} mv(\dot{\beta} + r) \\ m\dot{v} \\ J\dot{r} \end{bmatrix} = \begin{bmatrix} -\sin \beta & \cos \beta & 0 \\ \cos \beta & \sin \beta & 0 \\ 0 & 0 & 1 \end{bmatrix} \begin{bmatrix} F_x \\ F_y \\ M_z \end{bmatrix}$$

In these equations  $F_x$ ,  $F_y$  and  $M_z$  were obtained in the previous blocks where  $m, v$  and  $J$  are known parameters of the simulated vehicle.  $\beta$  is calculated in a recursive way. These equations form the Vehicle Dynamics Block which is shown in Figure 3.14.

This block takes  $F_x$ ,  $F_y$  and  $M_z$  as input arguments and calculates

- i.  $v$ : vehicle velocity (m/s)
- ii.  $\dot{\psi}$ : ( $\dot{\psi}$ ) yaw rate (rad/s)
- iii.  $\beta$  ( $\beta$ ): vehicle side slip angle

at its output.

The input output relations explained above are realized in Simulink as shown in Figure 3.14.

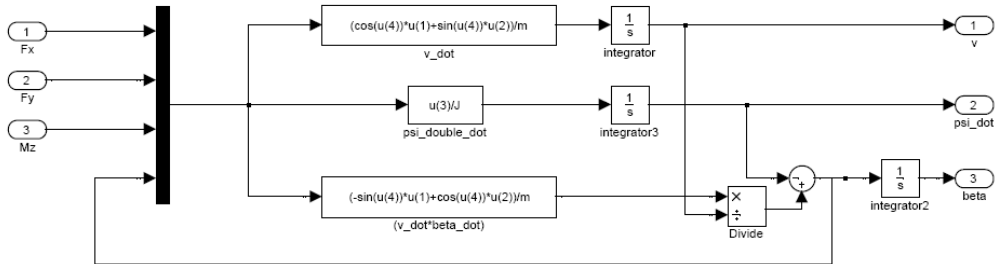


**Figure 3.14:** Simulink Implementation of the Vehicle Dynamics Equations

### Kinematics / Geometry Block

The vehicle considered as a rigid body has the constraint that each moving particle on the body has the same velocity both in x and y axes. This property is used to obtain the last set of equations required to complete the model.

$$V_f \cdot \cos \beta_f = V_r \cdot \cos \beta_r = V \cdot \cos \beta \quad (3.27)$$

Velocities on the x-axis are

$$V_f \sin \beta_f = V \sin \beta + l_f \dot{\psi} \quad (3.28)$$

and velocities on the y-axis are

$$V_r \sin \beta_r = V \sin \beta - l_r \dot{\psi} \quad (3.29)$$

Combining (3.28) and (3.29) and solving for  $\tan \beta_f$  and  $\tan \beta_r$  gives

$$\frac{V_f \sin \beta_f}{V_f \cos \beta_f} = \frac{V \sin \beta + l_f \dot{\psi}}{V \cos \beta} \quad \rightarrow \quad \tan \beta_f = \tan \beta + \frac{l_f \dot{\psi}}{V \cos \beta} \quad (3.30)$$

$$\frac{V_r \sin \beta_r}{V_r \cos \beta_r} = \frac{V \sin \beta - l_r \dot{\psi}}{V \cos \beta} \quad \rightarrow \quad \tan \beta_r = \tan \beta - \frac{l_r \dot{\psi}}{V \cos \beta} \quad (3.31)$$

The terms on the right side of these equations were already calculated in the previous blocks which will therefore be used as the known input arguments to obtain the unknown parameters  $\beta_r$  and  $\beta_f$  as shown in Figure 3.15.

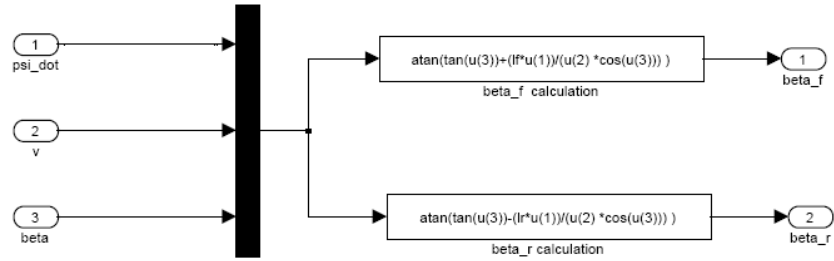


**Figure 3.15:** Simulink Implementation of the Kinematics Geometry Equations

### Simple Driver Model

A simple driver model is added to keep the longitudinal speed constant during simulations which is shown in Figure 3.16.

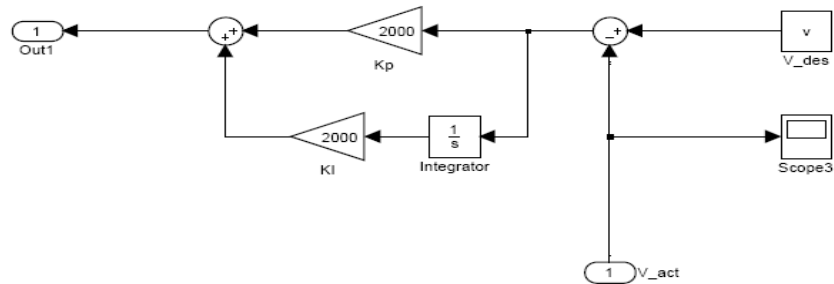


**Figure 3.16:** Simple Driver Model

The driver model consists of a PI controller that forces the vehicle to travel at a desired speed by producing additional force in the longitudinal direction which is then added to the  $F_x$  as shown in Figure 3.11.

### 3.1.4 Linear Single Track Model

For small values of  $\beta$  the nonlinear expressions explained in the previous section can be reduced by using :

$$\sin(\beta) \sim \beta \quad \text{and} \quad \cos(\beta) \sim 1$$

and for small steering angles the tires can be modelled by using linear equations. The linear single track model is shown in Figure 3.17.

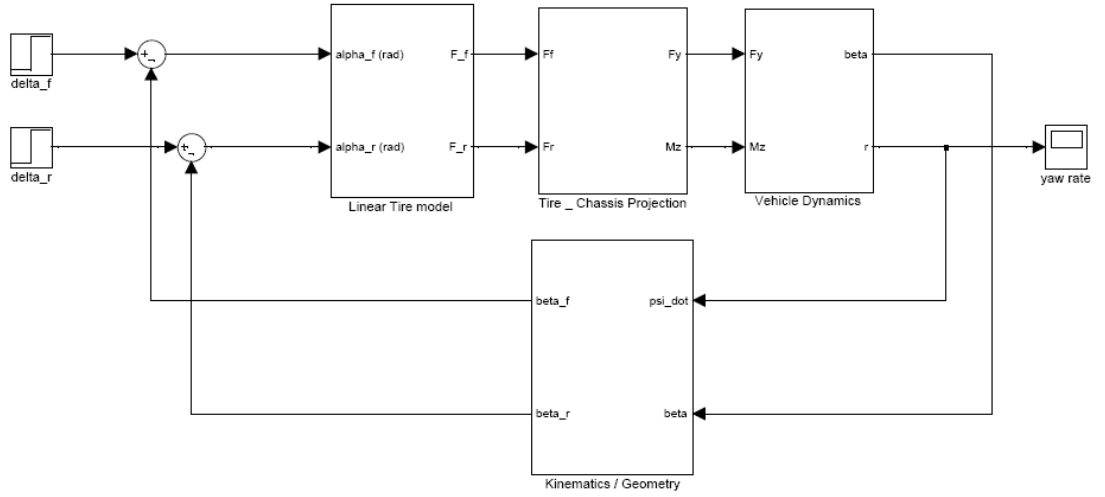


**Figure 3.17:** Linearized Single Track Model

#### Linear Tire Model

For small angles the tire forces can be expressed by using the following linear equations:

$$F_f = F_f(\alpha_f) = F_f(\delta_f - \beta_f) = C_{\alpha_f} \cdot \alpha_f \quad (3.32)$$

$$F_r = F_r(\alpha_r) = F_r(\delta_r - \beta_r) = C_{\alpha_r} \cdot \alpha_r \quad (3.33)$$

Which was modeled in Simulink as shown in Figure 3.18.

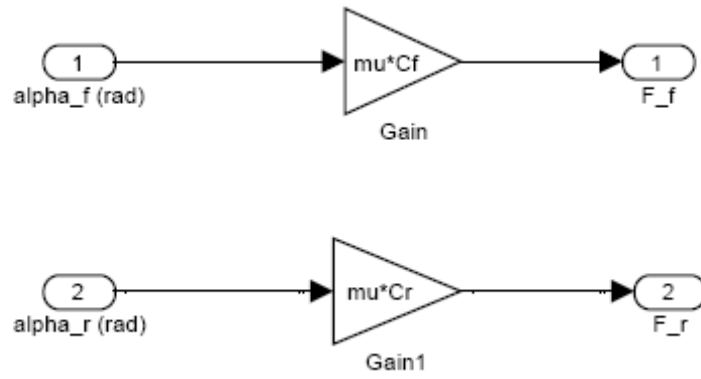


**Figure 3.18:** Simulink Linear Tire Model

### Tire Chassis Projection

The reduced tire chassis projection equations are obtained by taking  $\sin \delta \sim 0$  and  $\cos \delta \sim 1$  for small  $\delta$  which results in :

$$\begin{bmatrix} F_y \\ M_z \end{bmatrix} = \begin{bmatrix} 1 & 1 \\ lf & -lr \end{bmatrix} \begin{bmatrix} F_f \\ F_r \end{bmatrix} \quad (3.34)$$

Simulink implementation of (3.33) is shown in Figure 3.19.

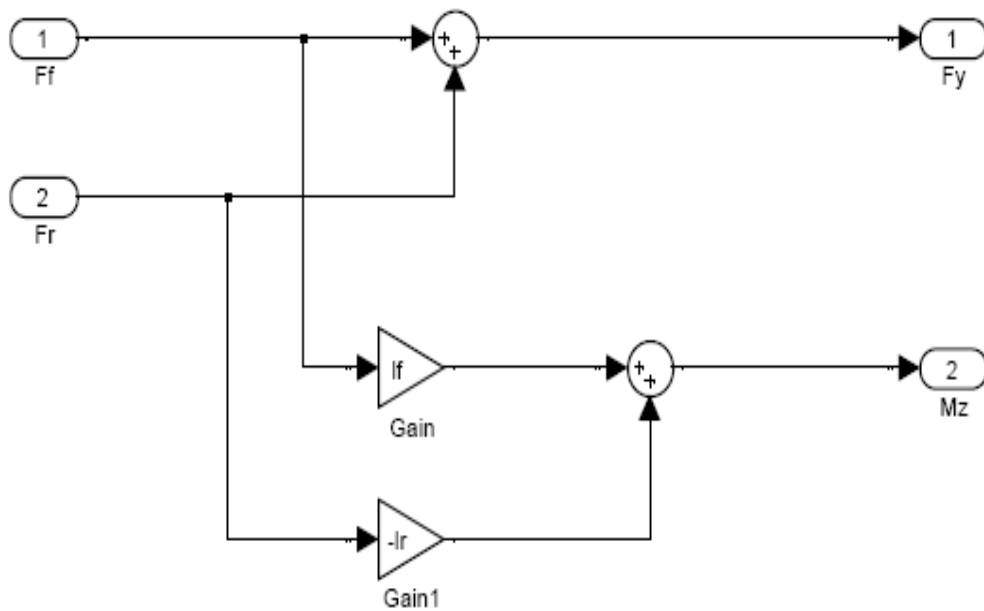


**Figure 3.19:** Linearized Tire/Chassis Projection Block



### Linearized Vehicle Dynamics

Linearized vehicle dynamics equations are given by:

$$\begin{bmatrix} F_y \\ M_z \end{bmatrix} = \begin{bmatrix} mv(\dot{\beta} + \dot{\psi}) \\ J\ddot{\psi} \end{bmatrix} \quad (3.35)$$

Simulink implementation is shown in Figure 3.20.

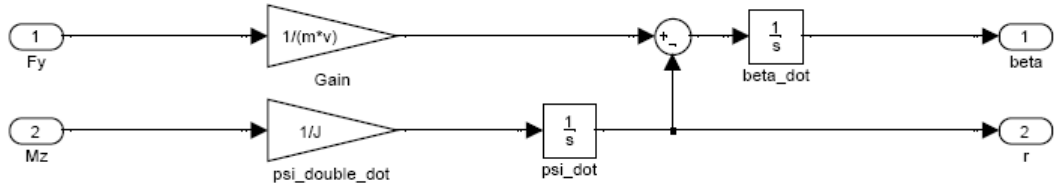


**Figure 3.20:** Simulink Implementation of the Linearized Vehicle Dynamics Block

### Kinematics / Geometry:

The Kinematics / Geometry block which was given in (3.30) and (3.31) is reduced by taking  $\sin(\beta) \sim \beta$ ,  $\cos(\beta) \sim 1$  and  $\tan(\beta) \sim \beta$  resulting in

$$\beta_f = \beta + \frac{l_f \dot{\psi}}{V} \quad (3.36)$$

and

$$\beta_r = \beta - \frac{l_r \dot{\psi}}{V} \quad (3.37)$$

respectively.

Simulink implementation of the linearized kinematics/geometry equations is shown in Figure 3.21.

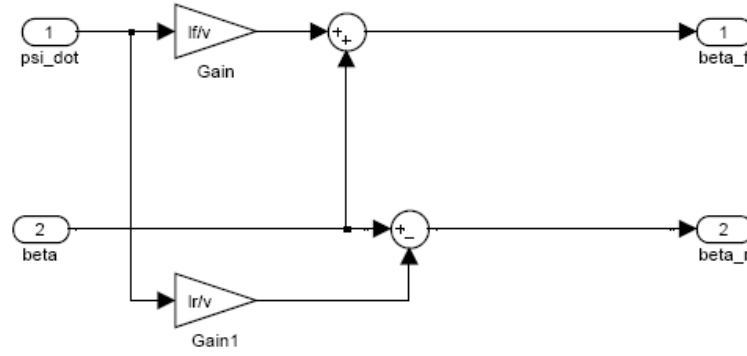


**Figure 3.21:** Simulink Implementation of the Linearized Kinematics Block

### 3.2 Steering System Model

The steering subsystem modeling used here is similar to the work in [10]. The steering subsystem is illustrated in Figure 3.22.

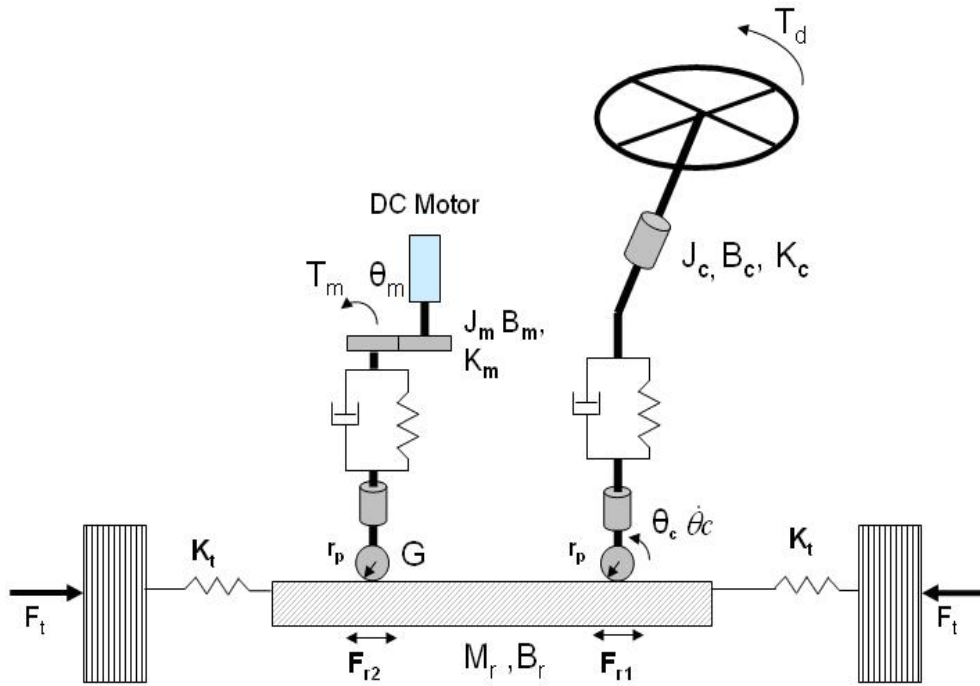


**Figure 3.22:** Schematic Representation of the Double-pinion Steering System

The parameters used in this model are presented in Table 3.2.

**Table 3.2:** Steering System Paramaters

Parameter	Explanation	Units
$J_c$	steering wheel & column moment of inertia	$\text{kgm}^2$
$K_c$	steering column torsional stiffness	Nm/rad
$B_c$	steering column damping	Nms/rad
$M_r$	rack mass	kg
$B_r$	rack damping	Nms/rad
$K_t$	tie or rack centering spring rate	Nm/rad
$F_{tr}$	tie-rod force (road disturbance input)	N
$r_p$	pinion radius	m
$G$	gear ratio (motor)	-
$J_m$	motor moment of inertia	$\text{kgm}^2$
$K_m$	motor and gearbox torsional stiffness	Nm/rad
$B_m$	motor and gearbox damping	Nms/rad
$k$	motor torque and voltage constant	Nm/A
$L$	motor inductance	Henry
$R$	motor resistance	Ohm

Lagrange's equations of motion are used in deriving the steering subsystem dynamic model. The kinetic energy of the steering subsystem is

$$\begin{aligned}
T_M &= T_{column} + T_{pinion2} + T_{rack} \\
&= \frac{1}{2} J_c \dot{\theta}_c^2 + \frac{1}{2} J_m \dot{\theta}_m^2 + \frac{1}{2} M_r \dot{x}^2
\end{aligned} \tag{3.38}$$

where  $\theta_c$  and  $\theta_m$  are the column and second pinion angular positions and  $\dot{x}$  is the rack velocity. The potential energy of the steering subsystem model is

$$\begin{aligned}
V &= V_{column} + V_{pinion2} + V_{rack} \\
&= \frac{1}{2} K_c \left( \theta_c - \frac{x}{r_p} \right)^2 + \frac{1}{2} K_m \left( \theta_m - \frac{xG}{r_p} \right)^2 + \frac{1}{2} K_t x^2
\end{aligned} \tag{3.39}$$

The Lagrangian of the system is

$$\begin{aligned}
L_M &= T_M - V_M \\
&= \frac{1}{2} J_c \dot{\theta}_c^2 + \frac{1}{2} J_m \dot{\theta}_m^2 + \frac{1}{2} M_r \dot{x}^2 - \frac{1}{2} K_c \left( \theta_c - \frac{x}{r_p} \right)^2 \\
&\quad - \frac{1}{2} K_m \left( \theta_m - \frac{xG}{r_p} \right)^2 - \frac{1}{2} K_t x^2
\end{aligned} \tag{3.40}$$

The application of Lagrange's equations given by

$$\frac{d}{dt} \left( \frac{\partial L}{\partial \dot{q}_i} \right) - \frac{\partial L}{\partial q_i} = Q_i \quad i=1,2,\dots,n \tag{3.41}$$

for the three generalized coordinates  $\theta_c$ ,  $\theta_m$  and  $x$  result in the three second order equations of motion

$$J_c \ddot{\theta}_c + B_c \dot{\theta}_c + K_c \left( \theta_c - \frac{x}{r_p} \right) = T_d \tag{3.42}$$

$$J_m \ddot{\theta}_m + B_m \dot{\theta}_m + K_m \left( \theta_m - \frac{xG}{r_p} \right) = T_m = ki \tag{3.43}$$

$$M_r \ddot{x} + B_r \dot{x} + K_t x = \frac{K_c}{r_p} \left( \theta_c - \frac{x}{r_p} \right) + \frac{K_m G}{r_p} \left( \theta_m - \frac{xG}{r_p} \right) + F_t \quad (3.44)$$

The steering rack position  $x$  is converted to tire steering angles for the left and right tires by tabulating the kinematic relation

$$\delta_{fl} = f_{fl}(x) \quad (3.45)$$

$$\delta_{fr} = f_{fr}(x) \quad (3.46)$$

Equations (3.44) and (3.45) are taken from [11] and are used in lookup table form in the Simulink implementation. The block diagram representation of the steering model in Equations (3.41)-(3.45) above is shown in Figure 3.23.

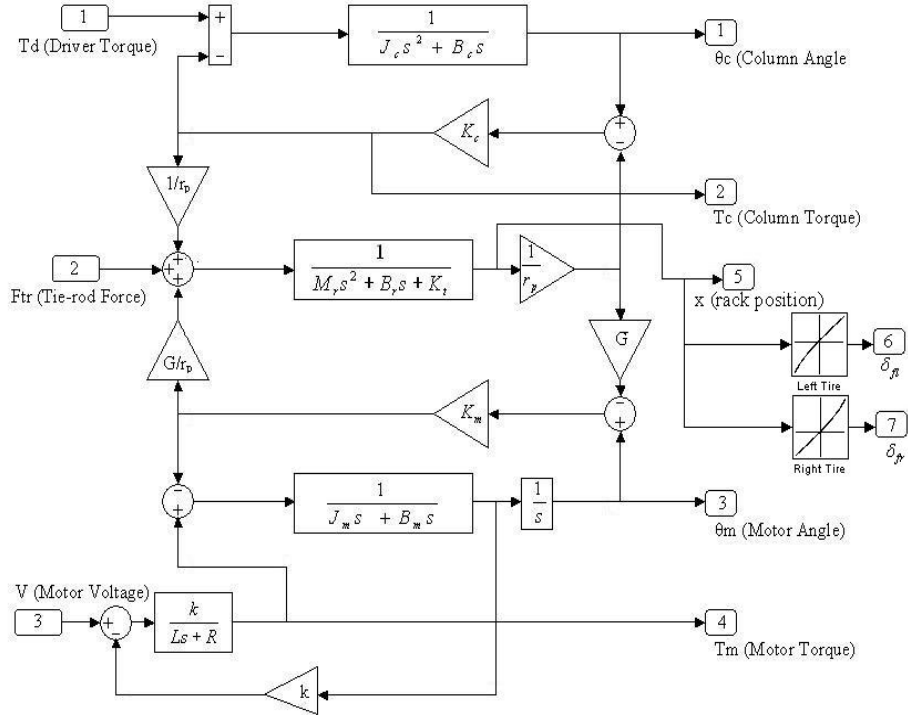


**Figure 3.23:** Steering system block diagram

## 4. EXPERIMENTAL SETUP

### 4.1 Steering Test Tig

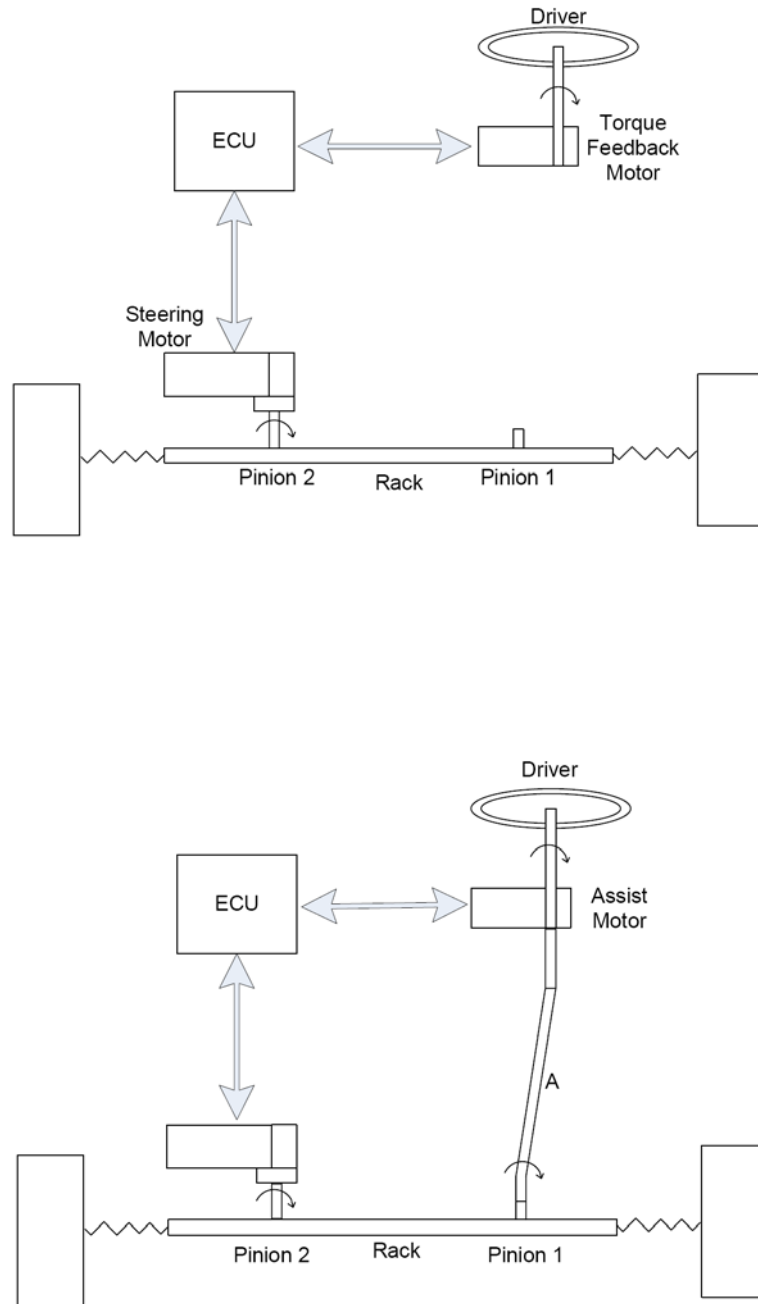
A modular steering test rig corresponding, in principal, to the steering subsystem of the Ford Transit Connect light commercial vehicle was prepared as a hardware-in-the-loop testbed. The test rig shown in Figure 4.1 has a modular structure which makes it possible to be used in both active steering and steer-by-wire configurations. There are two electric motors mounted on the test rig at present, one brushless and one brush-type d.c. motor. The electric motors used can be changed easily.



Figure 4.1: Steering Test Rig

The electric motor actuators are utilized for different tasks depending on the steering actuation method. In the steer-by-wire configuration Figure 4.2 (top) the d.c. motor mounted on the second pinion is used as the steering actuator while the motor on the steering column provides the driver torque feedback. In the electric power assisted

steering configuration, Figure 4.2 (bottom), the column motor provides the power assist to the driver while the motor on the second pinion is used to generate external disturbances and tire road forces in order to provide realistic driving conditions and to make controller performance examination possible. The setup can easily be converted from one configuration to the other by removing/mounting the mechanical connection between the steering column and the rack that is marked with “A” in Figure 4.2.



**Figure 4.2:** Different steering architectures that can be investigated using the steering test rig

The use of a steering test rig in a hardware-in-the-loop setup was motivated by several factors:

- Different electric motors can be tested easily in a laboratory hardware-in-the-loop setup as compared to retrofitting it in the test vehicle.
- It is possible to test conditions like icy road,  $\mu$ -split braking etc. which are difficult and expensive in road testing.
- It is also possible to design test scenarios that may not be possible to achieve in a road test.
- It is possible to inject soft sensor and actuator failures in a hardware-in-the-loop simulation without having to worry about safety.
- It is possible to easily test different steering concepts like electric power assisted steering, active steering and steer-by-wire by making small changes to a modular steer-by-wire system.
- Researchers can concentrate only on the steering system including its actuators, sensors and controller as the rest of the system exists as software and cannot fail during the tests.

## **4.2 Experimental Vehicle**

The experimental vehicle is the Ford Transit Connect light commercial vehicle with a double pinion steering rack. It is illustrated in Figure 3. The original hydraulic steering assist system was replaced with a double pinion steering rack formed by welding pinion holding halves of the left side and right side driver steering racks. A torque sensor and angular position sensor were added to the steering wheel assembly to measure driver steering torque and steering wheel position, respectively. A high power d.c. electric motor was connected to the extra pinion for generating extra steering torque. The servo driver for the d.c. electric motor can be used in both position and torque control modes. All control logic resides in a dSpace microautobox and rapidpro system.

The torque sensor and d.c. motor are used for electric power assisted steering during normal operation as manual no-assist steering is very difficult, especially during low speed driving and parking. In this mode of operation, the experimental vehicle has



programmed 'soft' and 'medium' steering wheel feel.

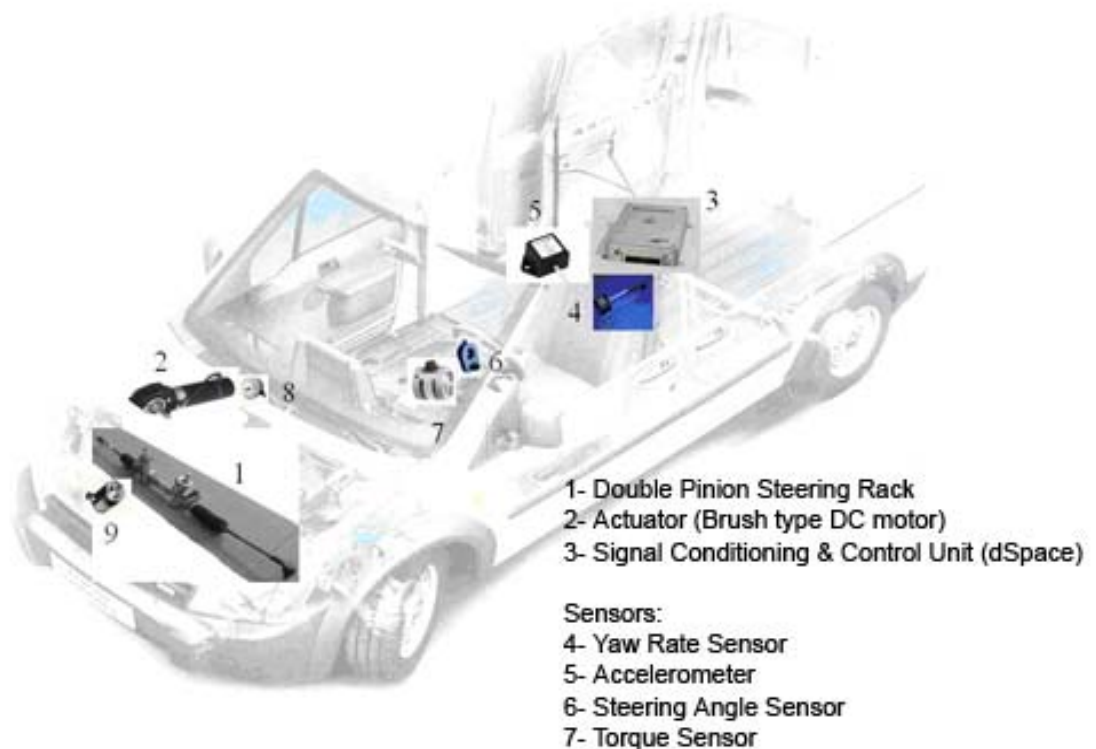


**Figure 4.3:** The Experimental Vehicle

For steer-by-wire and yaw stability control, the active steering d.c. motor is used in the position control mode. Controllers are developed in Simulink and tested using virtual models first. The experimental vehicle is used for final verification of the developed algorithms. Rapid controller prototyping is used. The controllers created as block diagrams in Simulink are converted to code and downloaded to the dSpace control system automatically.

### **4.3 Active Steering System Hardware**

In this section, hardware components of the active steering system will be presented. The electronic control unit consists of dSpace MicroAutobox and RapidPro systems.[12] The MicroAutobox is a powerful, compact, stand-alone prototyping unit with real-time hardware, I/O, and signal conditioning units. It provides an easy-to-use graphical interface for developing, testing, and optimizing control functions rapidly and reliably in real time. It is compatible with Matlab/Simulink and generates

embedded code automatically from models developed in Simulink. RapidPro system is used for signal conditioning purposes. For detailed technical specifications of MicroAutobox and RapidPro systems see Appendix A.



**Figure 4.4:** The Electronic Control Unit Implemented on the Experimental Vehicle

The double pinion steering rack and its packaging on the experimental vehicle is shown in Figure 4.5. The double pinion steering system has been manufactured by combining the steering racks of left side and right side steering racks. The steering column is connected to the left hand side and an electric motor is connected to the extra pinion on the right hand side. The hydraulic assist cylinder in the original vehicle is discarded in this approach. The original vehicle with HPAS also has a torsion bar used as a torque sensor that provides a torsional displacement proportional to the driver torque. In the modified active steering configuration, the torsion bar in each pinion is replaced by a torsionally stiffer bar. A steering wheel torque sensor replaced them in the active steering modification.



**Figure 4.5:** Double Pinion Steering Rack Mechanism

A 24 V DC (direct current) motor was used to generate the calculated torques on the rack mechanism. The DC motor and its driver used in the active steering system is shown in Figure 4.6.



**Figure 4.6:** DC Motor and Driver

The electrical motor was connected to the extra pinion on the double pinion mechanism. A tachometer was connected to the shaft of the electrical motor to obtain angular velocity information. Packaging of the electrical motor in the experimental vehicle is shown in Figure 4.7.



**Figure 4.7:** Electrical Motor Connection on the Experimental Vehicle

A steering wheel angular position sensor is used to obtain wheel position information. The sensor provides readings as CAN messages. These CAN messages can be read using MicroAutobox CAN module.



**Figure 4.8:** Steering Wheel Angular Position Sensor

To measure the torque applied by the driver, a torque sensor which gives  $\pm 10V$  analog output for  $\pm 50Nm$  torque is used. Output of the sensor is connected to the differential analog digital converter module on the RapidPro system. The instrumentation of the torque sensor on the experimental vehicle is shown in Figure 4.9.



**Figure 4.9:** Instrumentation of the Torque Sensor

A yaw rate sensor was instrumented on the vehicle to obtain vehicle yaw dynamics information which is essential for the yaw stability controller design.



**Figure 4.10:** Yaw Rate Sensor

## **5. ELECTRIC POWER ASSISTED STEERING**

The original Ford Transit Connect uses a hydraulic power assist system (HPAS) for steering. The current trend in the automotive sector is to replace hydraulic steering with electric steering. This is also called EPAS (electric power assisted steering). In EPAS, the hydraulic boost actuator is replaced by an electric motor providing the same boost torque to amplify the driver commands based on the steering boost curve. The main advantage of using EPAS over HPAS is that the expensive hydraulic system and the constant hydraulic pump load on the engine are not present in EPAS. This reduces the complexity of the steering system, reduces engine load and improves fuel efficiency. It is also easier to control EPAS electronically for electronically adjustable steering characteristics. A previous study on applying compliance control to EPAS has been conducted in Ford Otosan [11]. Since automotive companies are quite interested in using EPAS, there are also a correspondingly large number of references on EPAS modeling and control that appeared in recent years.

A review of the literature on EPAS system modeling and control will be presented first. In reference [13], control of an EPAS system is analyzed in two main parts: reduction of steering torque exerted by the driver and improvement of return-to-center performance of the steering system. The assist torque value is determined using a torque map which varies with vehicle speed, steering wheel angle and reference steering torque. Some simulations, hardware in the loop based experiments and some typical results were presented in this reference where a sensor which is capable of measuring both the steering torque and steering wheel angle was used. The authors showed that with the proper EPAS logic, the driver can turn the steering wheel with significantly reduced steering torque. A PI controller was used for steering torque reduction and a PID controller was used for improving return-to-center performance.

In reference [14], vehicle stability improvement using yaw rate sensor feedback in an electric power steering system was analyzed. It was shown that an EPAS system incorporating yaw rate sensor feedback helps stabilize the driver-vehicle system. A driver steering model is developed through control theoretic modeling of human



steering behavior. The assist torque varies with driver torque and yaw rate based on an algebraic equation.

In reference [15], a d.c. motor driven EPAS system integrating a manual rack and pinion steering system was investigated. The d.c. motor was connected to the steering system through a set of gears. The electronic controller used in that reference develops an output voltage that controls the d.c. motor, based on the vehicle speed and steering column torque inputs. The relation between angular displacement of the front wheel and the driver torque and the relation between the input motor voltage and the angular displacement of the front wheel were analyzed. The assist torque value varies with the vehicle speed and driver torque. A torque sensor was used to obtain the driver torque. The fact that the amount of assist torque needed at low speeds and park maneuvers is maximum and that the assist torque value decreases with increasing vehicle speed were demonstrated.

In reference [16], the  $H_\infty$  method, employing the boost curve to form a feedforward control, was used to design controllers for improved performance and robustness of the electrical power assist steering system. A dynamical model of a column assisted EPAS system was presented. The driver's torque command was not measured directly. Instead, a torque estimator was introduced to generate the driver's torque command. The boost curve of the assist torque varied with vehicle speed and driver torque.

In [17], an integrated EPAS control system with a full vehicle model was investigated. A column assisted steering system dynamic model was used. Electronic controller inputs were vehicle speed and driver torque. Driver torque was measured by a torque sensor which is located between the steering wheel and the electric motor. Co-simulations were carried out using the ADAMS and Matlab programs.

In reference [18], a double pinion type power assist steering system was analyzed dynamically. Relevant transfer functions that describe the assist dynamics, steering system compliance and driver road feel were presented. An assist torque-speed condition map was presented for actuator selection. Low speed parking and high speed random steer maneuvers were selected as worst case steering loads.

Active steering is available from suppliers [19] and is present in some production vehicles [20]. The available active steering systems have a clutch, which can engage or disengage the mechanical connection with the steering wheel. This is a fail safe approach as the mechanical steering system is in place in case of failure of the electric motor. Active steering can be used for implementing power steering, velocity dependent steering ratio or a yaw stability control system.

## 5.1 EPAS Controller Design

In this work, power assist is achieved by applying additional torque with the electrical motor through the extra pinion. The assist torque is calculated based on vehicle speed and driver steering torque. This is an open-loop approach which mimicks the operation of the hydraulic power assist system. The operation principle is shown in Figure 5.1.

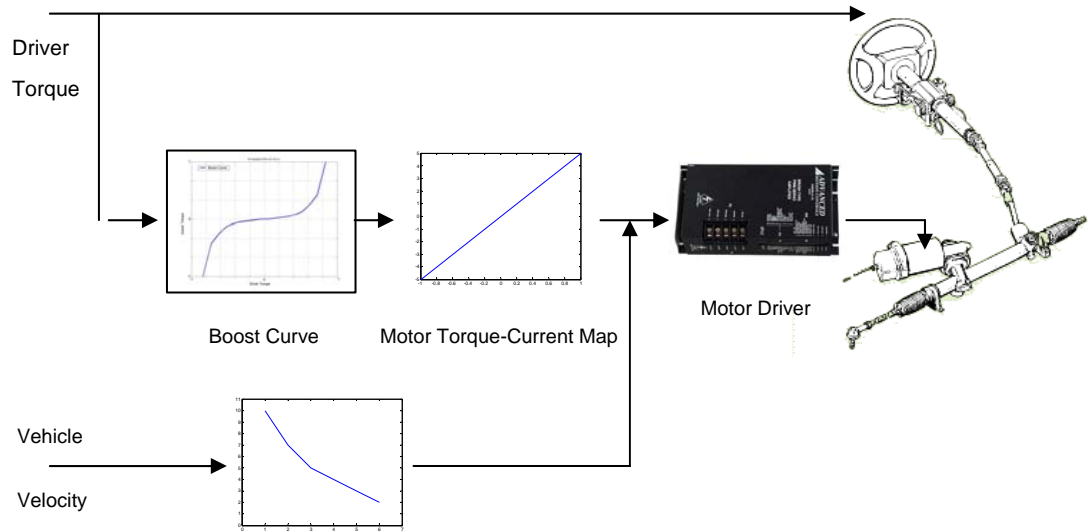


**Figure 5.1:** EPAS Controller Structure

The boost table is taken from [11] and is displayed in Figure 5.2.

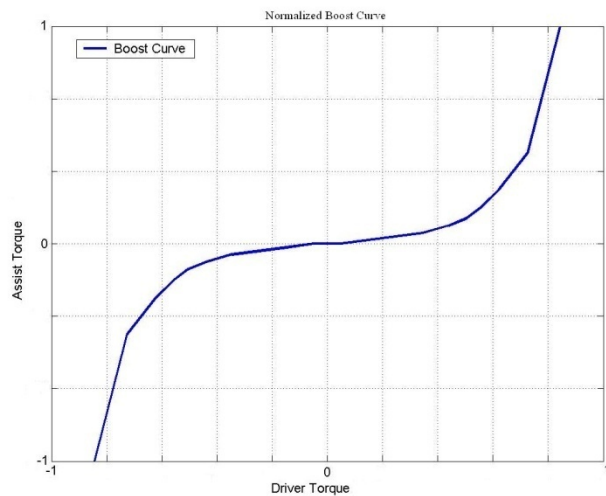


**Figure 5.2:** Normalized Boost Curve



## 6. STEER-BY-WIRE CONTROLLER DESIGN

Steer-by-wire systems possess only electrical connections between the steering wheel and the steering actuator. The full steering command is available to the controller. While steer-by-wire technology is presently available, it has not found application in production vehicles due to the lack of a mechanical backup system. Note that fly-by-wire systems have been used successfully for a long time in the aircraft industry. Consequently, steer-by-wire systems should also be expected to be commonly available components of future drive-by-wire vehicles after customer acceptance and regulatory compliance. The schematic representation of the steer-by-wire system is shown in Figure 6.1.

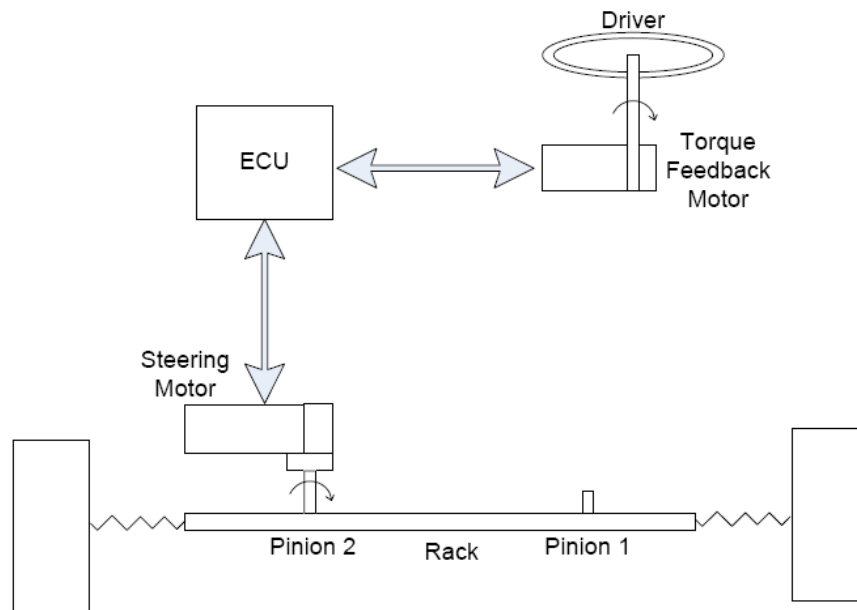


**Figure 6.1:** Schematic representation of steer-by-wire system

A hardware-in-the-loop setup was formed by integrating the vehicle models with the steering test rig. The steering system exists as hardware and the rest of the vehicle is implemented by software. A human driver closes the loop. The hardware-in-the-loop test setup is shown in Figure 6.2.

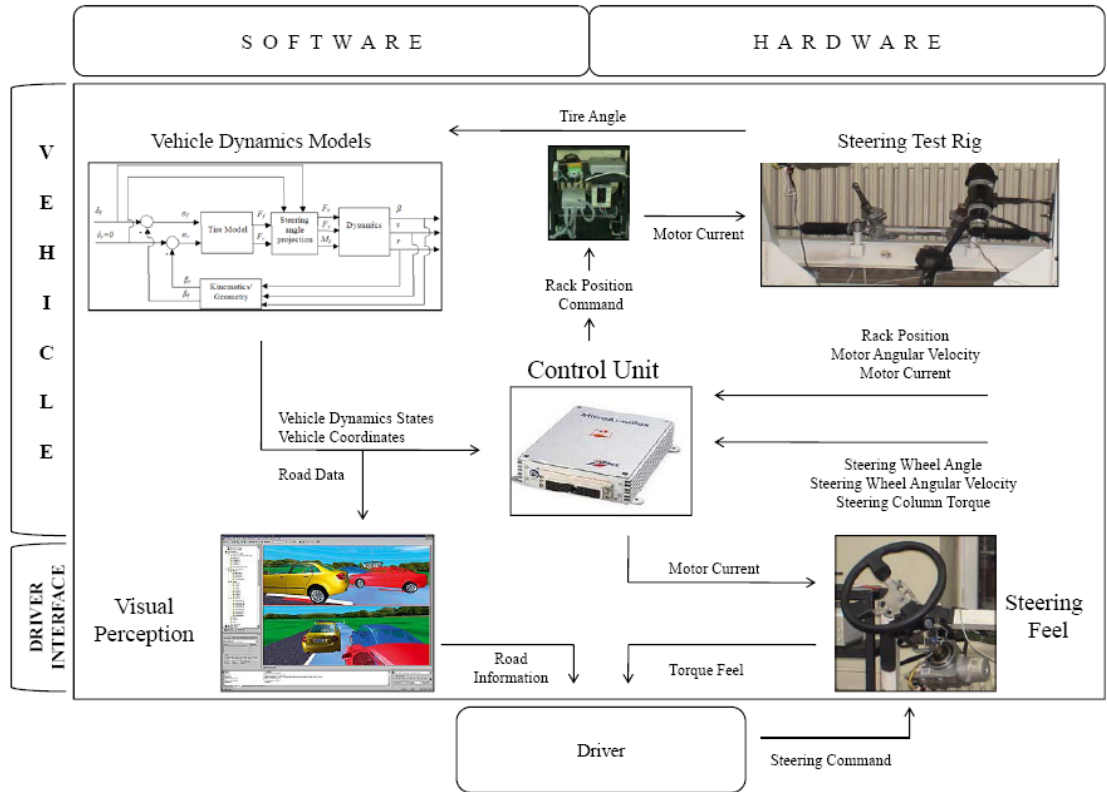


**Figure 6.2:** Schematic representation of steer-by-wire hardware-in-the-loop simulator components and their interactions

The steer-by-wire controller design involves design of two separate controllers. One of them is the steering command tracking controller and the other is a torque controller acting on the driver side in order to provide the driver with the desired steering feel in the absence of the mechanical linkage between the tires and the steering wheel.

This thesis focuses on the steering command tracking part of the steer-by-wire controller design. The position tracking controller is designed in a two loop structure as shown in Figure 6.3. One of them is an inner-loop compensator for robustness and the other is an external-loop compensator which satisfies desired performance specifications. The inner-loop compensator generates corrective control inputs in order to force an actual plant behave like its given nominal model. Once a well working inner-loop compensator is implemented the external-loop controller design can be carried out for the nominal model to meet the desired closed loop performance specifications [21].

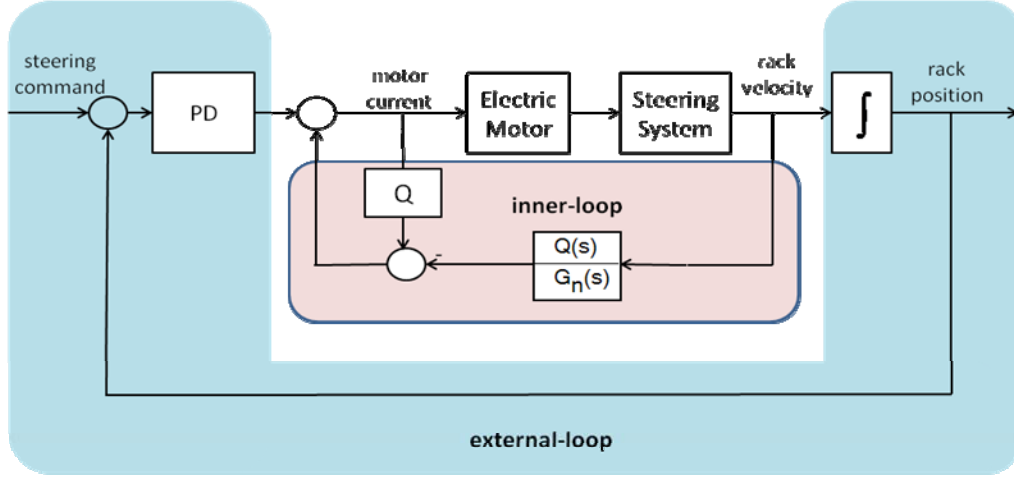


**Figure 6.3:** Two loop control structure

## 6.1 Disturbance Observer Based Steer-By-Wire Controller Design

In this thesis, a disturbance observer is implemented as the inner-loop compensator which forces the actual plant with parameter variations to follow a nominal model with known parameters which were identified experimentally in a relatively linear operating region. The external-loop compensator is a PD type position controller which places the closed loop poles of the system into a  $D$ -stable region in the complex plane where desired steering command tracking performance is satisfied.

### 6.1.1 Disturbance Observer

The disturbance observer is a method of designing a two degree of freedom control architecture to achieve insensitivity against modelling errors due to model order reduction and linearization, parameter uncertainties, sensor noise and external disturbances [22, 23]. Unlike its name, disturbance rejection is not the only feature of a disturbance observer. Its model regulation capability allows specification and achievement of desired system dynamics which was applied to the vehicle yaw stability control problem in [24, 25].

The steering system is subject to nonlinear friction effects, varying road friction, road disturbances, actuator rate limits and sensor noise. For the controller to be robust, a disturbance observer based model regulator was implemented in the inner-loop. The structure of the disturbance observer is shown in Figure 6.4.

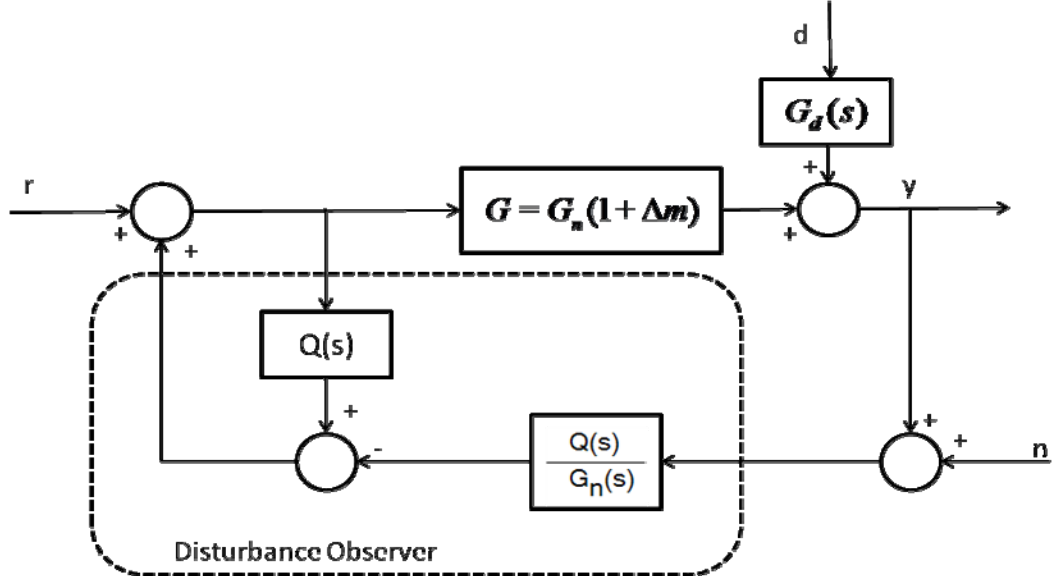


**Figure 6.4:** Disturbance Observer

The loop gain of the disturbance observer compensated plant is:

$$L = \frac{GQ}{G_n(1-Q)} \quad (6.1)$$

with the model regulation, disturbance rejection, and sensor noise rejection transfer functions given by:

$$\frac{y}{r} = \frac{G_n G}{G_n(1-Q) + GQ} \quad (6.2)$$

$$\frac{y}{d} = \frac{G_d}{1+L} \equiv G_d S = \frac{G_n(1-Q)G_d}{G_n(1-Q) + GQ} \quad (6.3)$$

$$\frac{y}{n} = \frac{-L}{1+L} \equiv -T = \frac{-GQ}{G_n(1-Q) + GQ} \quad (6.4)$$

In (6.3) and (6.4),  $S$  and  $T$  are the sensitivity and complementary sensitivity, functions, respectively.  $Q$  must be a low pass filter with unity d.c. gain. This choice of  $Q$  results in  $y/r \rightarrow G_n$  which is the desired steering dynamics,  $y/d \rightarrow 0$  (disturbance rejection) at low frequencies where  $Q \rightarrow 1$ . At higher frequencies where there may be considerable sensor noise,  $y/n \rightarrow 0$  (sensor noise rejection) will be achieved as  $Q \rightarrow 0$ . This choice of  $Q \rightarrow 0$  at higher frequencies is also necessitated by

the robustness of stability. Then the input-output behavior of the controlled system including its steady-state behavior will be the same as that of the nominal (or desired) model  $G_n$  up to the bandwidth of the low pass filter  $Q$  (steering system regulation along with good disturbance rejection).

In this study, the  $Q$  filter was chosen to be the simple low pass filter

$$Q(s) = \frac{1}{\tau_Q s + 1} \quad (6.5)$$

The electrical characteristics of electric motor which are effective at very high frequencies can be neglected when compared with the steering inputs of the driver (0~5 Hz). Also with rigid connections between the electric motor and the pinion, the steering system transfer function from motor current to rack angular velocity can be reduced to the following form :

$$G = \frac{\omega(rad / s)}{I(A)} = \frac{K_T}{J_T s + B_T} \quad (6.6)$$

Where  $J_T$ ,  $B_T$ ,  $K_T$  represent the total inertia, damping and gain of the system respectively. Parameter identification was carried out in high gain operating regions to minimize nonlinear friction effects. The system is excited with pulse current inputs and motor angular velocity measured from the tachometer is recorded as the output. The estimated first order transfer function is:

$$G_n = \frac{\omega(rad / s)}{I(A)} = \frac{9.8286}{s + 3.34} \quad (6.7)$$

which was taken as the nominal model for the disturbance observer design. An appropriate cutoff frequency for the  $Q$  filter is the bandwidth of the actuator which is 3 Hz. Figure 6.5 shows comparison of the experimental data with the estimated transfer function output subject to the same input current values. After the disturbance observer (DO) is activated, the outputs are nearly identical. Another test was performed to inspect model regulation performance at an operating point far away from the operating point used in linear model derivation. This operating point is selected in a region where nonlinear friction effects are effective. The experimental result presented in Figure 6.6 shows the disturbance observer performance.

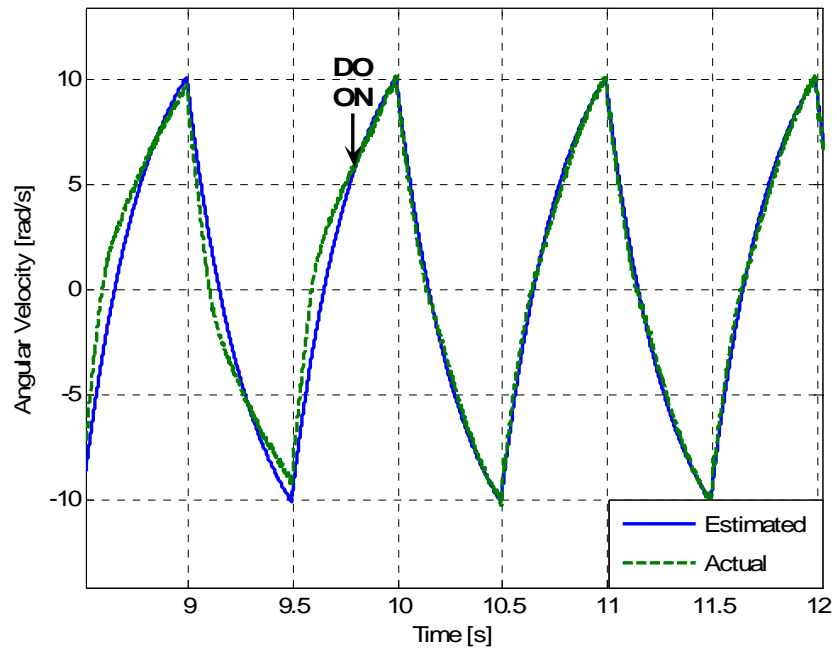


**Figure 6.5:** Model regulation performance of disturbance observer in high gain operating region

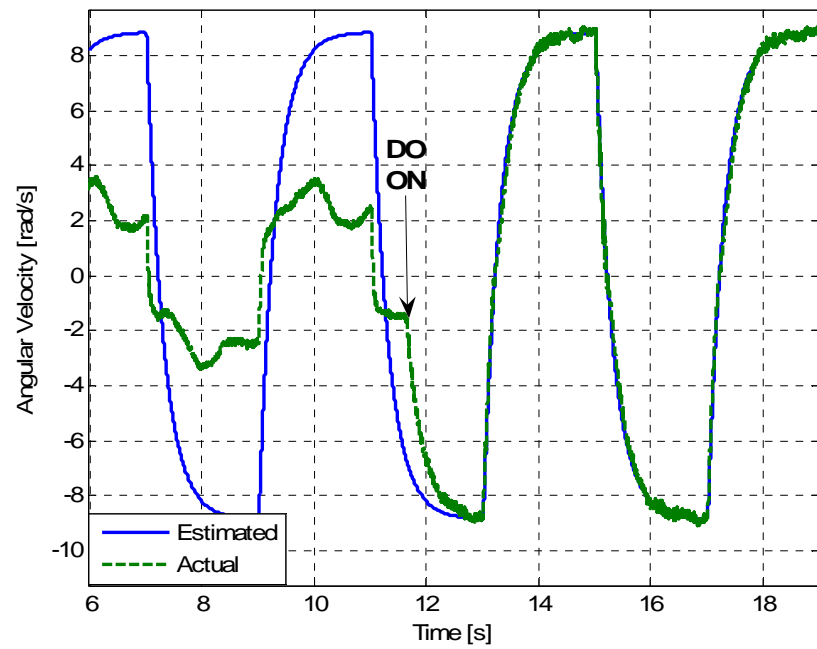


**Figure 6.6:** Model regulation performance of disturbance observer in a highly nonlinear region

### 6.1.2 *D*-Stable Position Controller Design

The next step in the steer-by-wire controller design is the design of the external-loop compensator which is a reference tracking controller. The controller was chosen as a PD type controller since the disturbance observer used already has a built-in integrator effect.

In the *D*-stability region of Figure 6.7, the condition that should be satisfied by the roots of the characteristic polynomial is that they lie inside the specified *D*-region. The *D*-region is defined by three parameters.  $\sigma$  defines the minimum real part when the root is close to origin, and the angle  $\theta$  defines a minimum damping value while the value  $R$  defines a maximum absolute value for the roots such that the controller bandwidth can be limited. The *D*-stability boundaries are formed by assuming the roots to be no closer than 3 to the imaginary axis and no further than 7 from the imaginary axis. A minimum damping ratio of  $\zeta=0.5$  is also assumed for generating the controller parameter space solution regions.

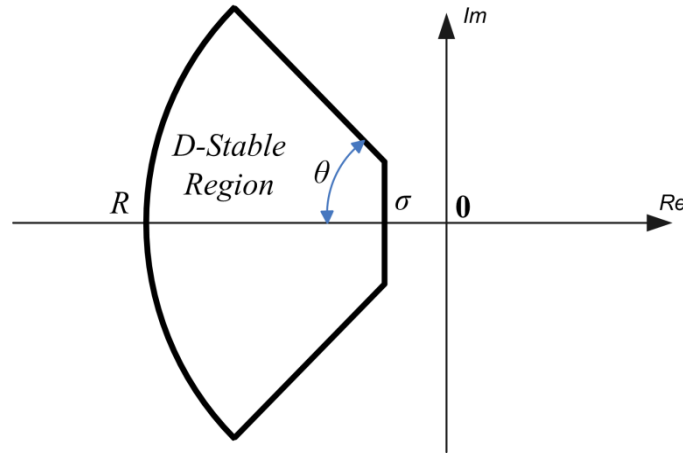


**Figure 6.7:** *D*-stable region in the complex region

The PD controller design task is to determine the set of all controller parameters  $(K_p, K_d)$  for which the nominal system is *D*-stable. This problem was solved using the parameter space approach [3]. The boundary of the *D*-region is mapped into the  $K_p, K_d$  plane. Figure 6.8 shows the *D*-stable boundaries in the calculated  $(K_p, K_d)$  plane. All controllers with  $K_p$  and  $K_d$  chosen inside the closed region satisfy given closed loop specifications.

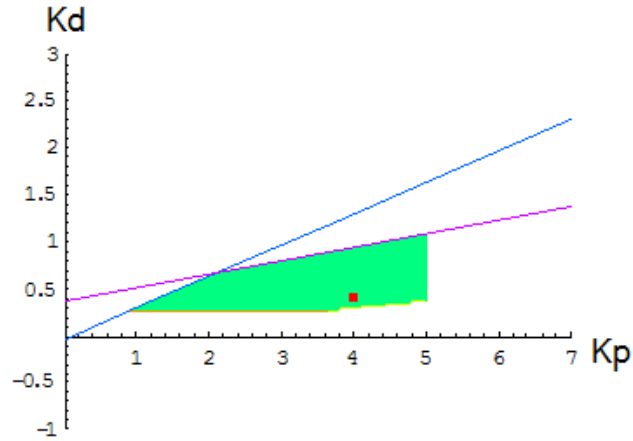


**Figure 6.8:** The Solution Region

The point marked with a dot in Figure 6.8 shows the controller parameters that are chosen as the specific solution to be used in the hardware-in-the-loop simulations. To test the controller performance together with the disturbance observer, a step steering input reference tracking simulation was performed in the hardware-in-the-loop setup. The steering command tracking performance is shown in Figure 6.9.

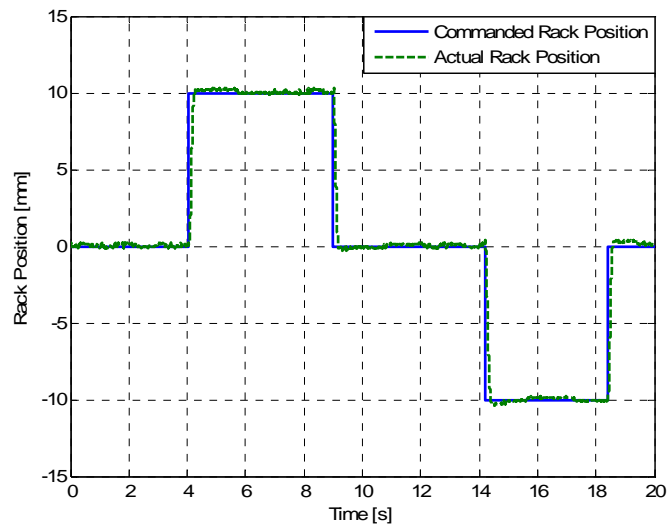


**Figure 6.9:** Step response of the steer-by-wire controller



## **7. YAW STABILITY CONTROLLER DESIGN**

Driver assistance systems based on active safety technology assist the driver in avoiding potentially hazardous situations by taking over control authority temporarily to provide corrective action during the panic reaction time of the driver. Yaw stability control of road vehicles is an important driver assistance system and is available commercially . Yaw stability controllers are starting to become a standard like ABS as their benefit in helping the driver and avoiding accidents is better understood. Presently available commercial yaw stability controllers use differential braking technology as the ABS and traction control hardware is already available for implementation. Steering actuation based yaw stability control is also possible and is available commercially in the form of active steering where the mechanical linkage between the steering wheel and the steering rack is kept in place, but an electric steering actuator is used to complement the mechanical driver input. The highest benefit from steering actuated yaw stability control can be achieved when steer-by-wire technology is used. In a steer-by-wire system, there is no mechanical connection between the steering wheel and the steering rack. Currently, production vehicles with true steer-by-wire do not exist, even though the steer-by-wire solution has been available for some time. One reason for this unavailability is the fact that customers do not place a high demand for steer-by-wire at present.

### **7.1 Disturbance Observer Based Steering For Yaw Stability Control**

The yaw stability controller used here is based on the disturbance observer architecture as in [24,25]. The block diagram of the disturbance observer based yaw stability controller is shown in Figure 7.1.

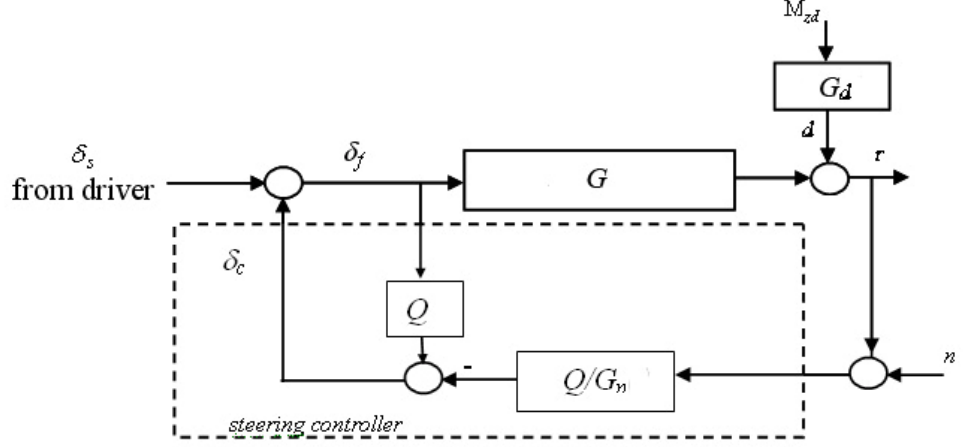


**Figure 7.1:** Disturbance observer based yaw stability controller block diagram

The loop gain of the yaw stability controller compensated plant is

$$L = \frac{G_{r\delta_f} Q}{G_n (1 - Q)} \quad (7.1)$$

with the steering model regulation, lateral disturbance rejection, and sensor noise rejection transfer functions being given by

$$\frac{r}{\delta_s} = \frac{G_n G}{G_n (1 - Q) + GQ} \quad (7.2)$$

$$\frac{r}{M_d} = \frac{G_d}{1 + L} \equiv G_d S = \frac{G_n (1 - Q) G_d}{G_n (1 - Q) + GQ} \quad (7.3)$$

$$\frac{r}{n} = \frac{-L}{1 + L} \equiv -T = \frac{-GQ}{G_n (1 - Q) + GQ} \quad (7.4)$$

In (7.3) and (7.4),  $S$  and  $T$  are the sensitivity and complementary sensitivity functions, respectively. The choice of  $Q$  as a low pass filter with unity d.c. gain results in  $r/\delta_s \rightarrow G_n$  which is the desired steering dynamics (steering model regulation) and  $r/M_{zd} \rightarrow 0$  (disturbance rejection) at low frequencies where  $Q \rightarrow 1$ . At higher frequencies where there may be considerable sensor noise,  $r/n \rightarrow 0$  (sensor noise rejection) will be achieved as  $Q \rightarrow 0$ . This choice of  $Q \rightarrow 0$  at higher frequencies is also necessitated by the robustness of stability requirement. Then, the

input-output behavior of the controlled system including its steady-state behavior will be the same as that of the nominal (or desired) model  $G_n$  up to the bandwidth of the low pass filter  $Q$  (steering model regulation along with good disturbance rejection).

In this study, the  $Q$  filter was chosen to be the simple low pass filter

$$Q(s) = \frac{1}{\tau_Q s + 1} \quad (7.5)$$

The desired yaw dynamics model was chosen to be the first order system given by

$$G_n(s, v) = \frac{K_n(v)}{\tau_n s + 1} \quad (7.6)$$

In (7.6)  $K_n(v)$  is the velocity scheduled single track model static gain. Two design parameters in the steering actuated disturbance observer are chosen as  $\tau_Q$  in (7.5) and  $\tau_n$  in (7.6). These two parameters form the controller parameter space used in design in the next section.

## 7.2 Multi-Objective Parameter Space Design

The model parameters that vary the most and are, therefore, crucial for robustness are road-tire friction coefficient  $\mu$  and the vehicle speed  $v$ . Figure 7.2 displays the region in the  $\mu$ - $v$  plane where yaw stability controller design objectives should be satisfied. Six representative design points marked with cross signs in Figure 4 are used in the design procedure.

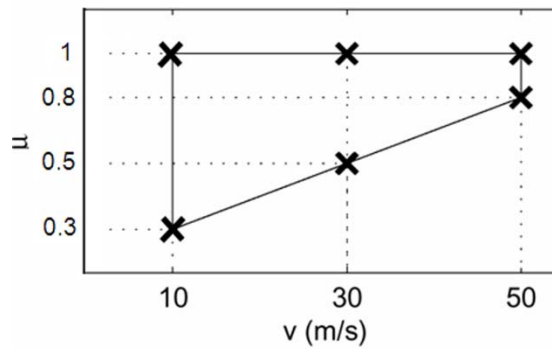


**Figure 7.2:** Region of uncertain parameters

Different control objectives are evaluated at each of these representative points to obtain corresponding  $\tau_n - \tau_Q$  controller parameter space regions. Graphical intersection of all six solution regions in the  $\tau_n - \tau_Q$  parameter space results in the solution region where the chosen objective is satisfied at all six design points. Multi-objective design is achieved by graphically intersecting parameter space solution regions for each objective. Three objectives are chosen here. They are satisfaction of  $D$ -stability, mixed sensitivity and parameter space bounds.

A typical  $D$ -stability region is shown in Figure 7.3. The  $D$ -stability boundaries are formed by assuming roots no closer than 0.8 to the imaginary axis and no further than 7 from the imaginary axis. A maximum damping of 80 degrees corresponding to a damping ratio of  $\xi = 0.17$  is also assumed for generating the solution regions.

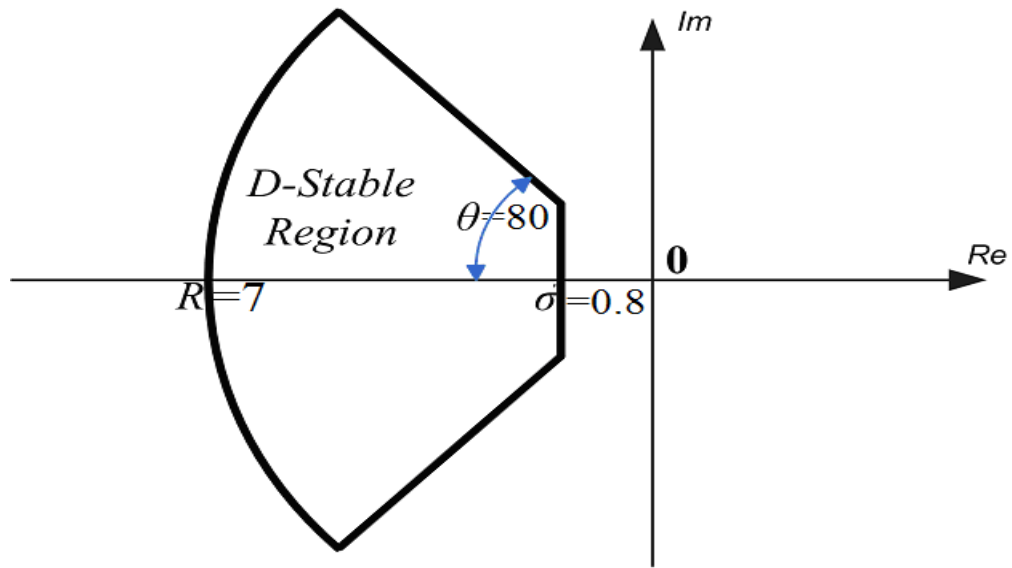


**Figure 7.3:**  $D$ -stability region in the complex plane

The  $D$ -stability regions corresponding to the six design points of Figure 7.2 are given in Figure 7.4 where the solution regions are shaded. The overall solution region which combines all solution regions in Figure 7.4 is shown in Figure 7.5. The combined solution region in Figure 7.5 satisfies the  $D$ -stability conditions.

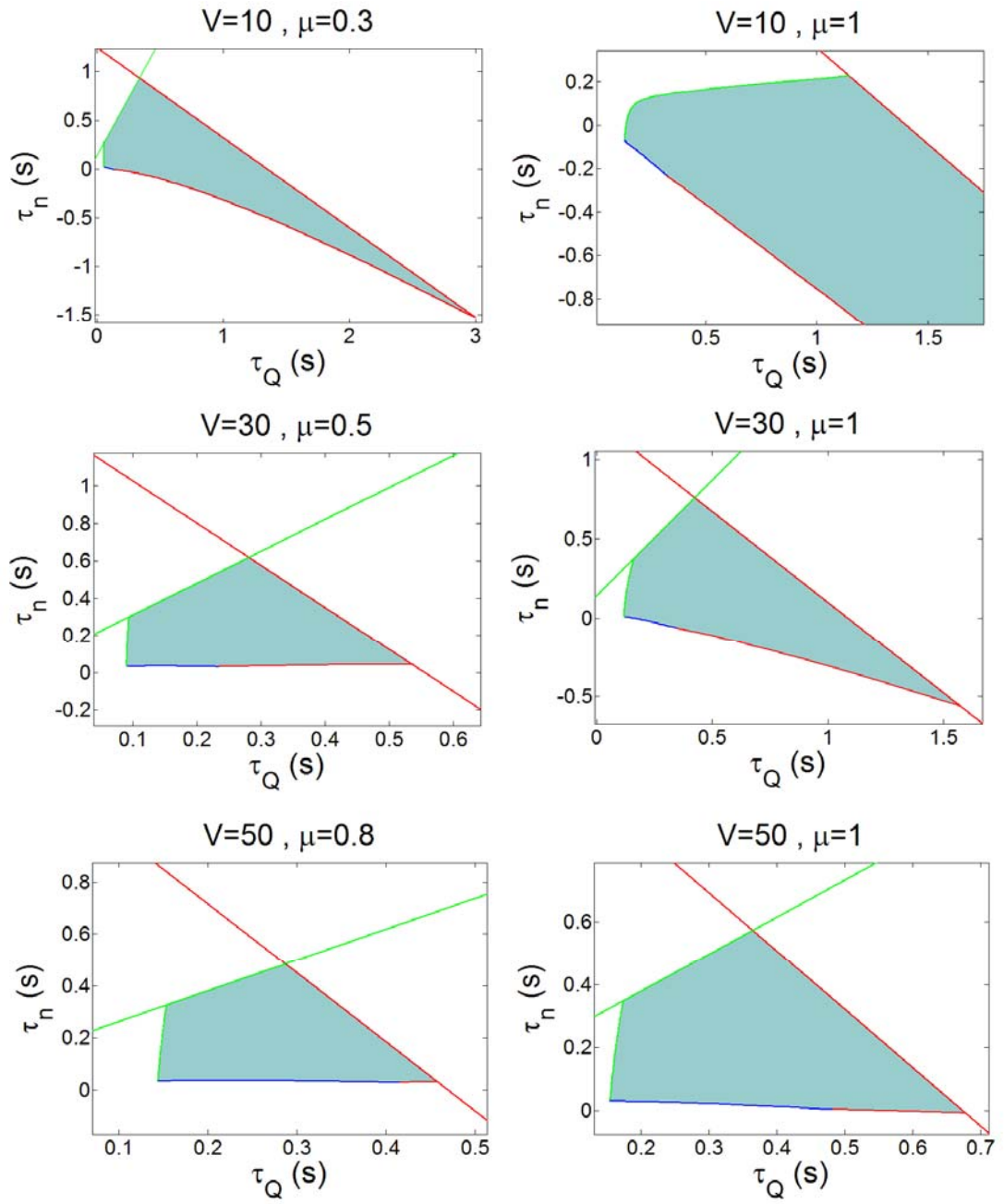


**Figure 7.4:**  $D$ -stability regions for the six design points

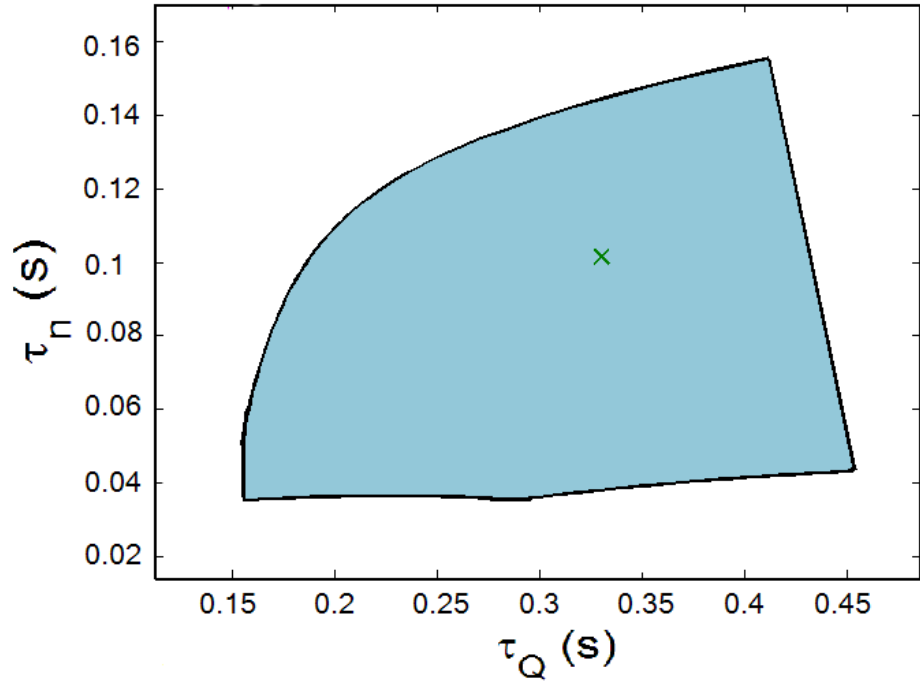


**Figure 7.5:** Overall  $D$ -stability region

A phase margin that is larger than  $40^\circ$  is the second objective that is chosen for the design. The combined solution region for the phase margin bound is shown as the shaded area in Figure 7.6.

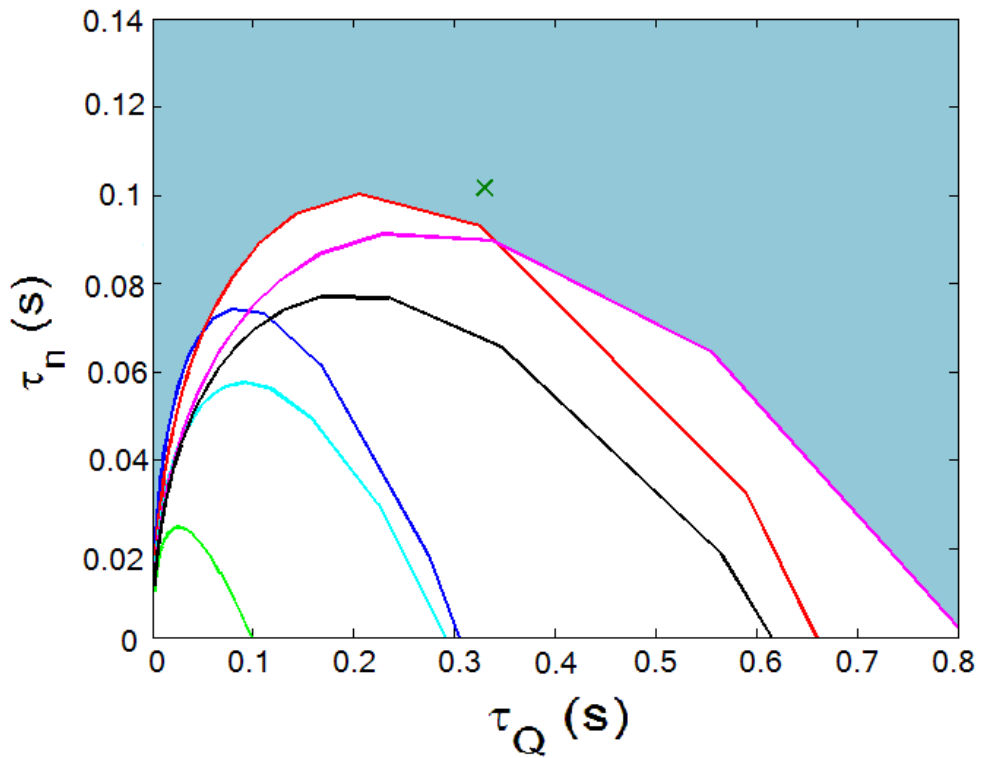


**Figure 7.6:** Phase margin bounds and combined solution area for operating points

The third objective is to map a mixed sensitivity  $H_\infty$  norm bound

$$|W_S S| + |W_T T| < 1 \text{ for } \forall \omega \quad (7.7)$$

to the  $\tau_n - \tau_Q$  disturbance observer parameter space region [27]. The sensitivity weights in (7.7) are:

$$W_S = h_S \frac{s + \omega_S l_S}{s + \omega_S h_S}, \quad W_T = h_T \frac{s + \omega_T l_T}{s + \omega_T h_T} \quad (7.8)$$

where  $l_S = 0.5$ ,  $h_S = 4$  and  $\omega_S = 3$  rad/s are for the sensitivity transfer function and  $l_T = 0.1$ ,  $h_T = 1.5$  and  $\omega_T = 20$  rad/s are for the complementary sensitivity transfer function. The solution method was explained in detail in Chapter 2. It was shown that controller parameters can be found by,

$$L = KG = (K_R + jK_I)G \quad (7.9)$$

Which now becomes

$$L = KG_{r\delta_f} = (K_R + jK_I)G_{r\delta_f} \quad (7.10)$$

where  $G_{r\delta_f}$  is the transfer function from the front wheel steering angle  $\delta_f$  to the yaw rate  $r$  which can be given by:

$$G_{r\delta_f}(s, v) = \frac{r(s)}{\delta_f(s)} = \frac{b_1(v)s + b_0(v)}{a_2(v)s^2 + a_1(v)s + a_0(v)} \quad (7.11)$$

with

$$\begin{aligned} b_0 &= c_f c_r (l_f + l_r) v \\ b_1 &= c_f l_f m v^2 \\ a_0 &= c_f c_r (l_f + l_r)^2 + (c_r l_r - c_f l_f) m v^2 \\ a_1 &= (c_f (I_z + l_f^2 m) + c_r (I_z + l_r^2 m)) v \\ a_2 &= I_z m v^2 \end{aligned} \quad (7.12)$$

And  $L$  is the loop gain which is:

$$L = \frac{G_{r\delta_f} Q}{G_n (1-Q)} \quad (7.13)$$

Solving (7.10) for the real and imaginary parts  $K_R$  and  $K_I$  of  $K$  and then solving

$$K_R + jK_I = \frac{Q}{G_n (1-Q)} \quad (7.14)$$

for  $\tau_n$  and  $\tau_Q$  results in

$$\tau_n = -\frac{K_R}{K_I \omega} \quad (7.15)$$

$$\tau_Q = -\frac{1}{K_n K_I \omega} \quad (7.16)$$

which is the final step in the solution. The mixed sensitivity solution regions are shown in Figure 7.7. The multi-objective solution regions of  $D$ -Stability, phase margin and mixed sensitivity bounds being mapped to the  $\tau_n$ - $\tau_Q$  disturbance observer parameter space are shown for the six design points in Figure 7.8.

The overall multi-objective design region formed by intersecting all regions in Figure 7.8 is displayed in Figure 7.9. The point marked with a cross (see also Figures 7.4-7.8) shows the controller parameters that are chosen as the specific solution to be used in the offline and real time simulations of the next section.



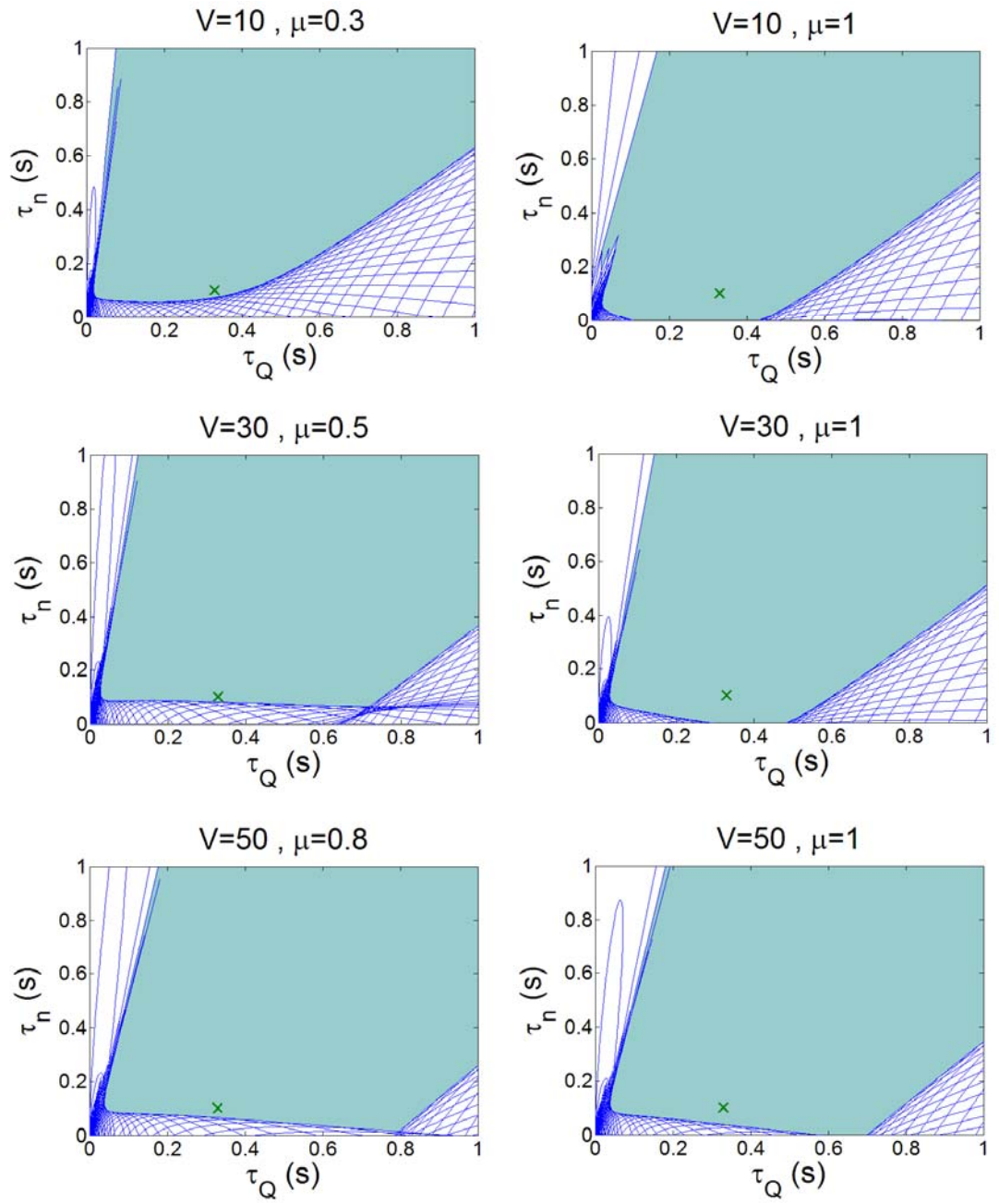


**Figure 7.7:** Mixed sensitivity solution regions for the six design points

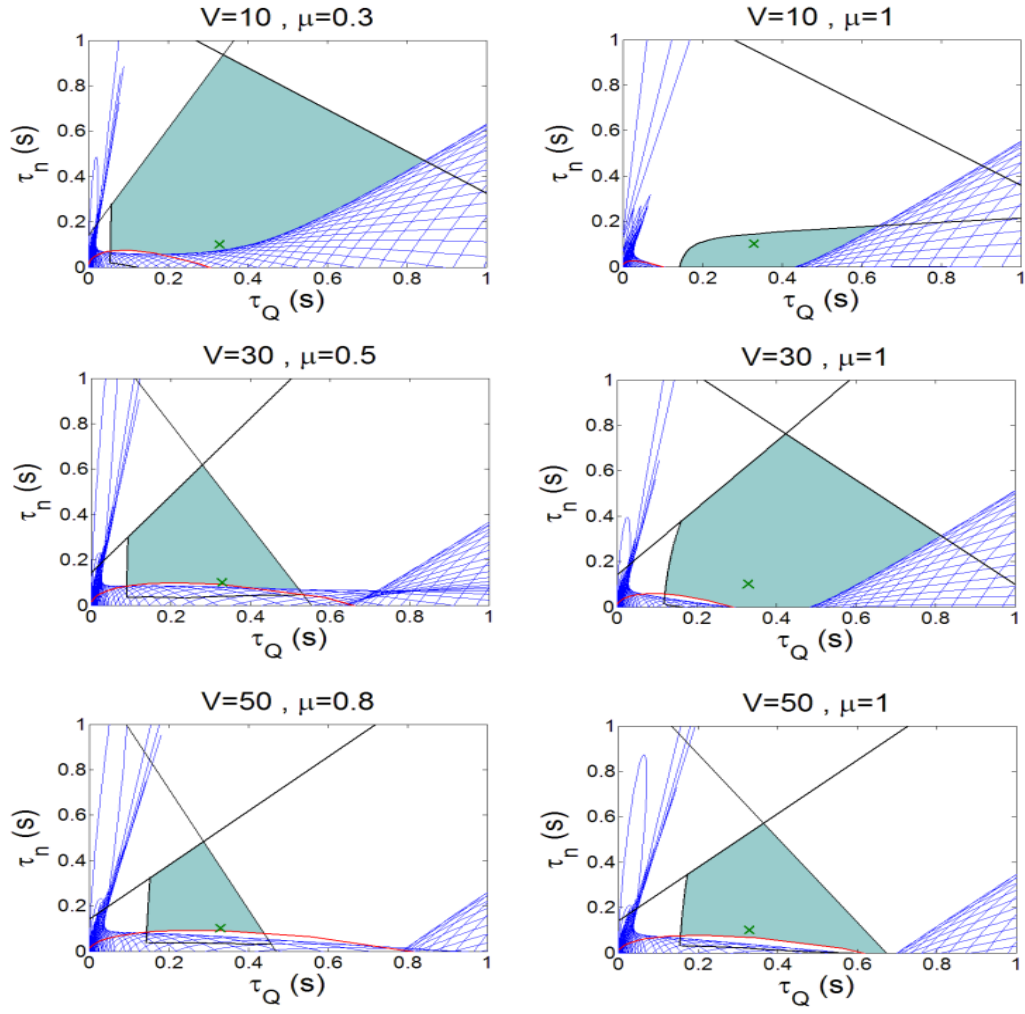


**Figure 7.8:** Combined solution regions for the six design points

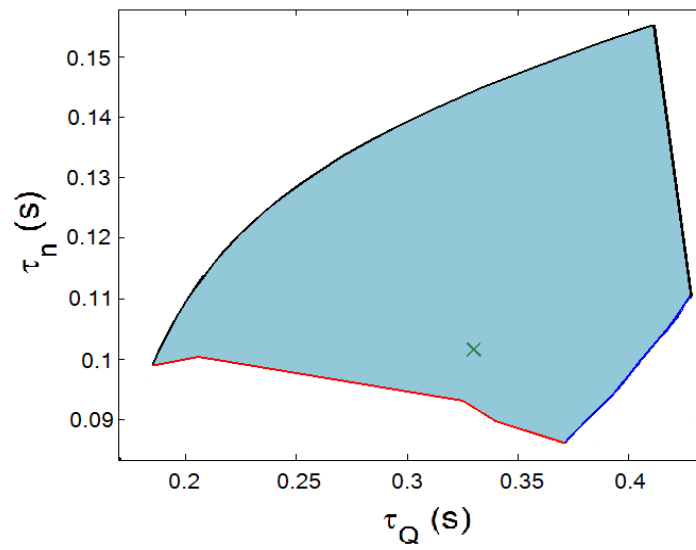


**Figure 7.9:** Overall multi-objective solution region

### 7.3 Simulation Studies

The first simulation result shown in Figure 7.10 is the steering wheel step input response of the nonlinear double track model with and without model regulator based yaw stability controller. The velocity is  $v=30$  m/s and the road friction coefficient is  $\mu=0.5$  corresponding to wet road. The controlled and desired yaw rate responses are almost identical demonstrating that good steering model regulation is achieved. The desired yaw rate response corresponds to the vehicle response under dry conditions. In contrast, the uncontrolled yaw rate response is far off from the desired response.

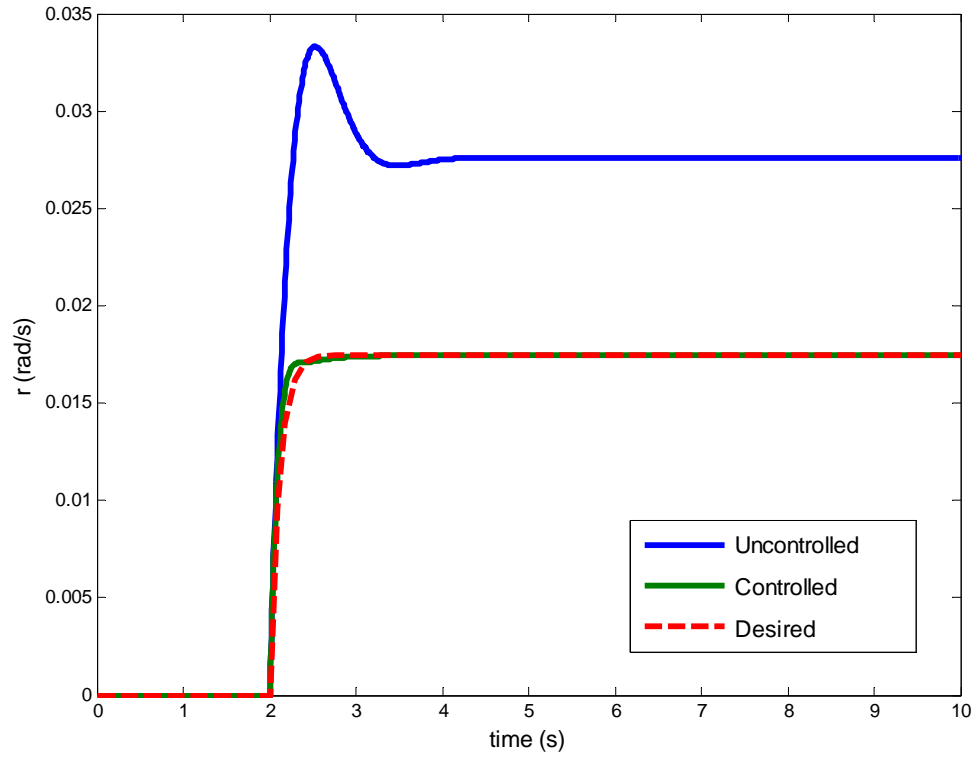


**Figure 7.10:** Step steering wheel inputs to uncontrolled and controlled models

In the second simulation, a step yaw moment disturbance  $M_{zd}$  was applied to the system at the same conditions of  $v=30$  m/s and  $\mu=0.5$ . The simulation result displayed in Figure 10 illustrates the enhanced yaw moment disturbance rejection made possible by the yaw stability controller. The corresponding stroboscopic plot of Figure 11 shows the difference in disturbance rejection more clearly.

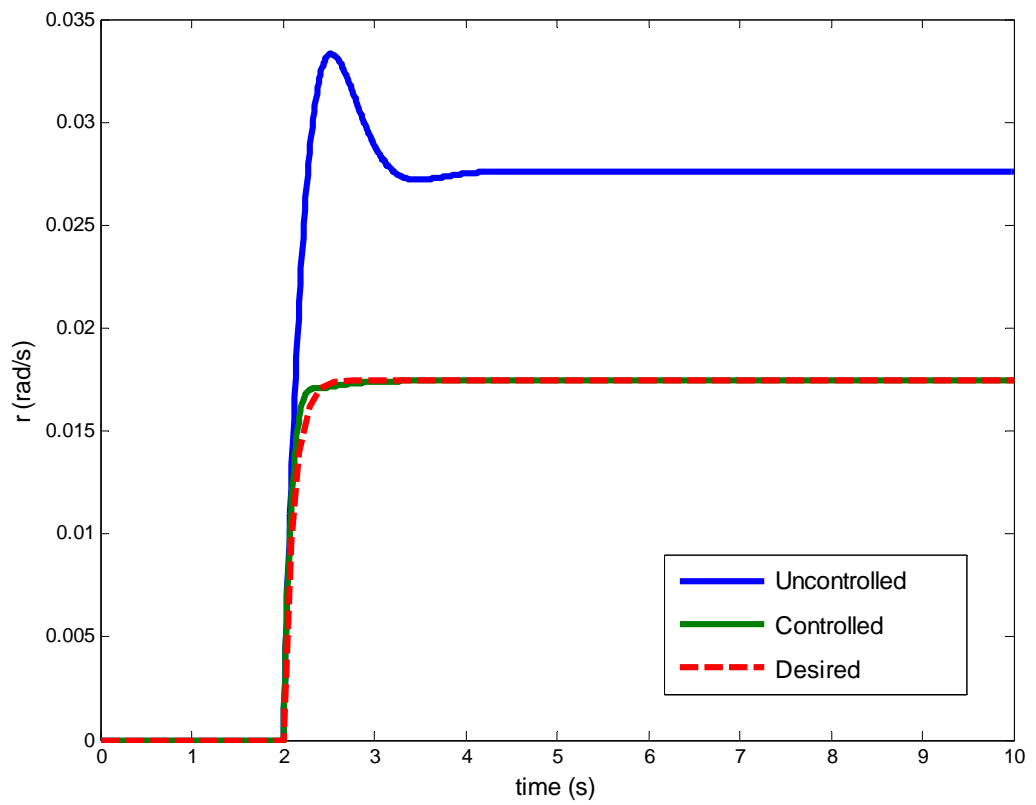


**Figure 7.11:** Step steering wheel inputs to uncontrolled and controlled models

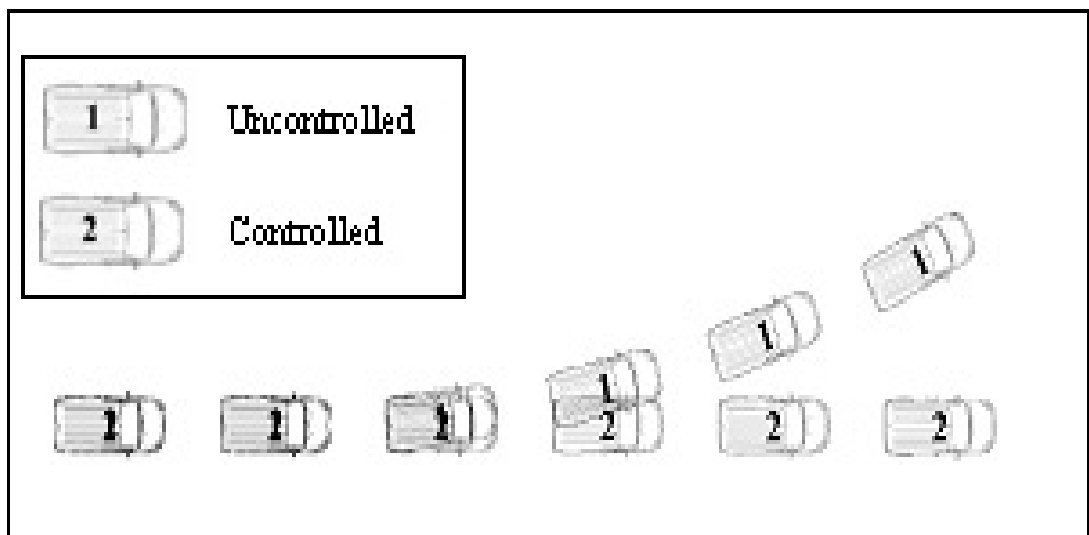


**Figure 7.12:** Stroboscopic plot

## 7.4 Hardware-in-The-Loop Test Setup

In this thesis, disturbance observer based vehicle yaw stabilization with steering actuation is realized through the steer-by-wire implementation. Figure 7.13 shows the schematic diagram of the hardware-in-the-loop setup used. Four types of simulations are used to assess the yaw stability controller performance, effect of actuator dynamics and hardware-in-the-loop performance. They are offline simulation without yaw stability control, offline simulation with yaw stability control, offline simulation with yaw stability control and an actuator dynamics model and hardware-in-the-loop simulation with yaw stability control.

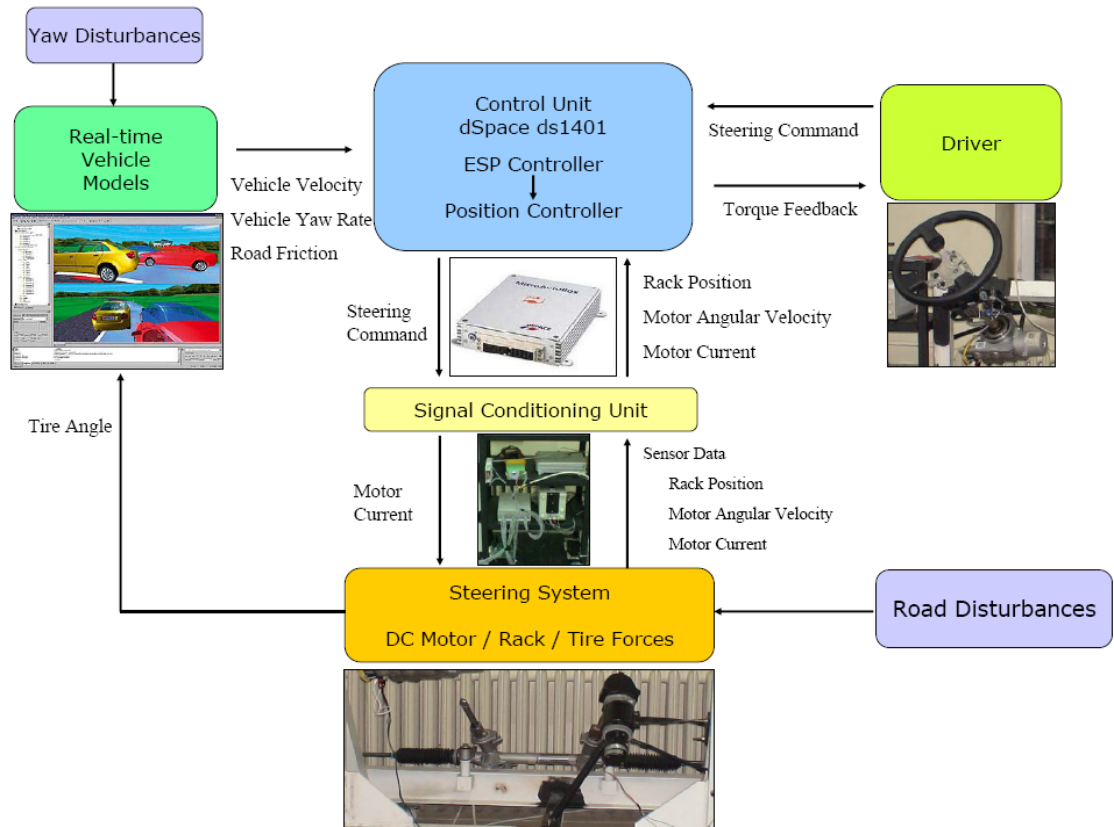


**Figure 7.13:** Schematic representation of steer-by-wire hardware-in-the-loop simulator components and their interactions

All four simulation types are subject to the same driving conditions, driver inputs and disturbances. In the hardware-in-the-loop simulations, vehicle dynamics are implemented as software that runs in real time. The yaw stability controller obtains the required vehicle dynamics information from the software model and commands the corrective steering actions to the actual steering actuator. The low level position

controller of the steering system receives the steering command and drives the steering electric motor to bring the rack to the desired position. The rack position is converted to the corresponding tire angle by using a look up table. Yaw stabilization through steering actuation requires precise positioning of the tire angles. For this purposes the steering command tracking controller developed for steer-by-wire system is used which was explained in Chapter 6.

The first hardware-in-the-loop simulation result shown in Figure 7.14 is the steering wheel step input response of the nonlinear single track vehicle model explained in Chapter 2 with three of the four different simulation types explained in the beginning of this section. In the second simulation in Figure 7.15, a step yaw moment disturbance was applied. The simulation results displayed in Figure 7.14 illustrate the satisfactory following of the desired steering step input while the results displayed in Figure 7.15 demonstrate excellent disturbance rejection. The steering actuator commanded by the yaw stability controller and the actual steering action output in the hardware-in-the-loop simulation are shown in Figure 7.16 during yaw moment disturbance rejection. Commanded and actual steering actions are seen to be almost identical.

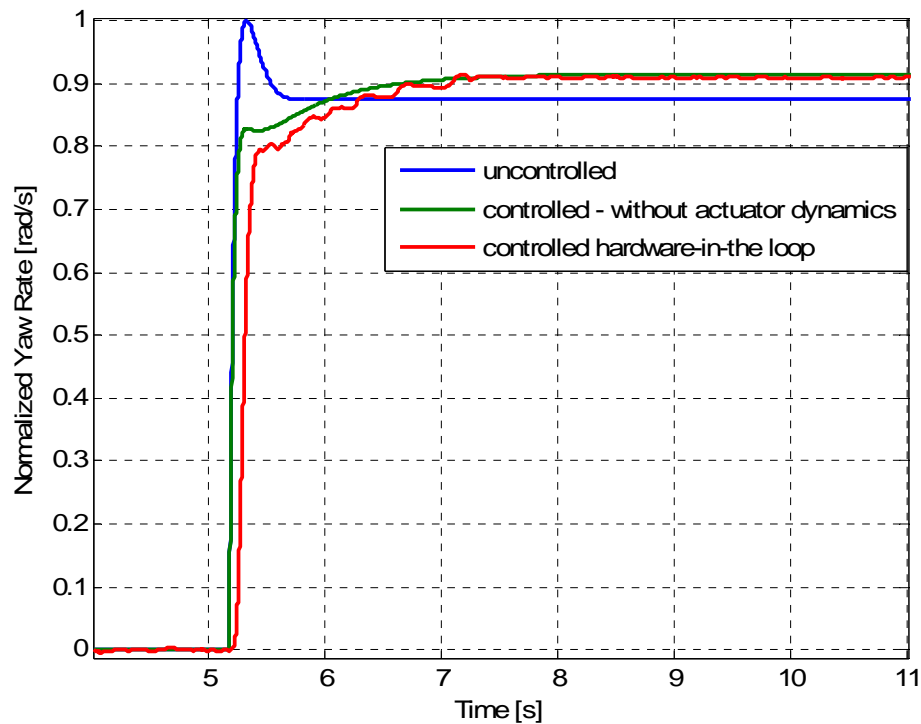


**Figure 7.14:** Step steering command input response simulation (normalized)

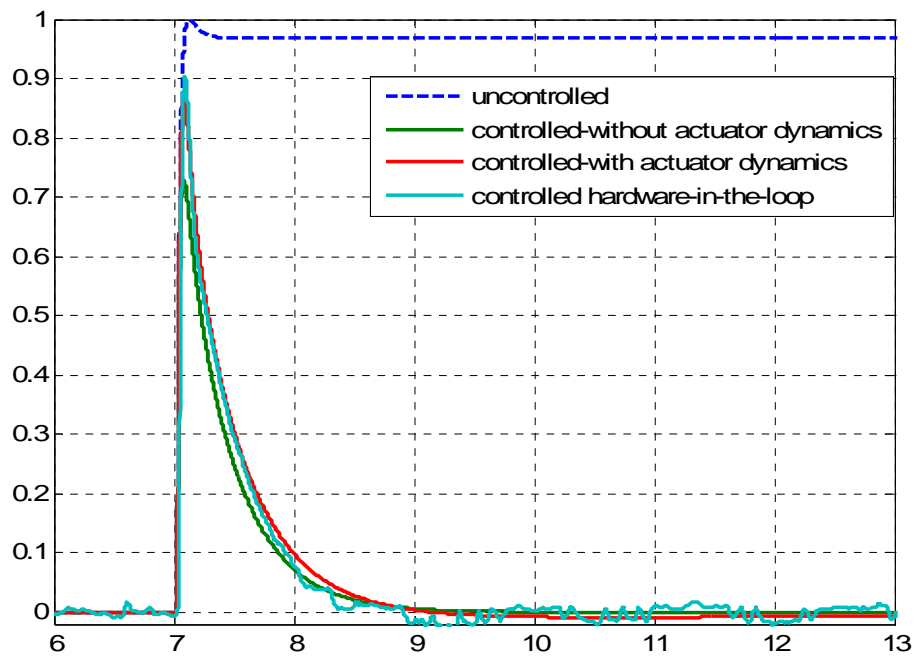


**Figure 7.15:** Step yaw moment disturbance simulation (normalized)

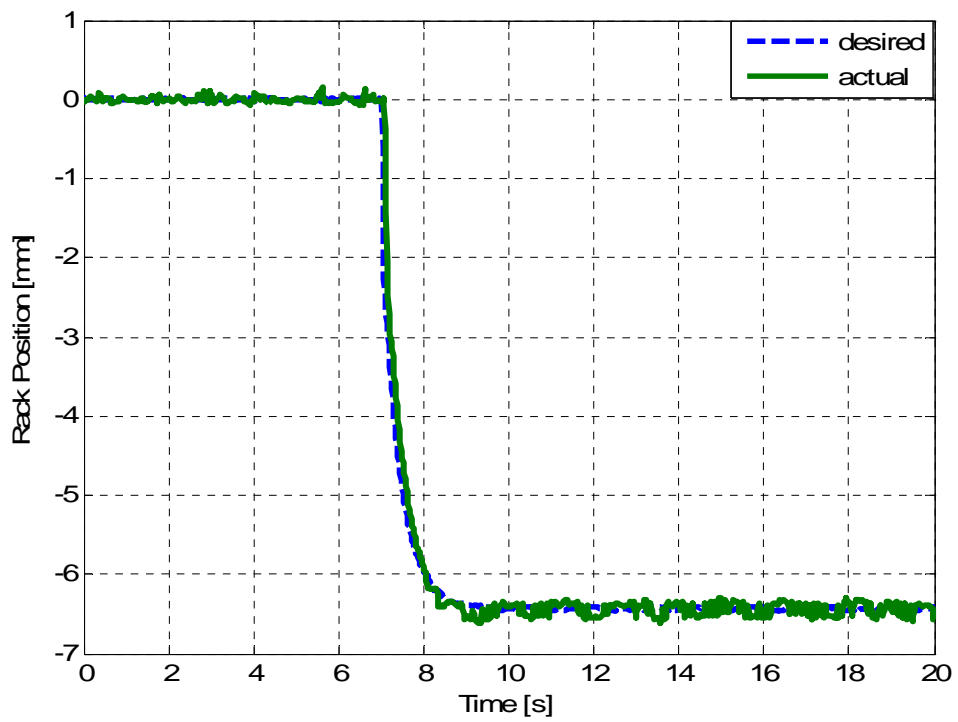


**Figure 7.16:** Commanded and actual steering actuator action

## 8. FINAL CONCLUSION

The main focus of this thesis was to design active steering controllers for a light commercial vehicle and their implementation. The study was carried out first by developing vehicle models and designing the active steering controllers based on these models. A prototype vehicle was instrumented with active steering system hardware and road tests were performed to validate the developed vehicle models. A steering test rig identical to the steering system on the actual vehicle was developed in a laboratory environment to test and tune the controllers before implementing on the actual vehicle. The first controller was an electrical power assisted steering system which was implemented on the actual vehicle and gave satisfactory results. The second active steering controller was a steer-by-wire controller. The test rig was used for experimental verification of the steer-by-wire controller designed here. The controller design used a two loop architecture. The inner loop had a disturbance observer control system used to improve the dynamics of the steer-by-wire system and to make it robust with respect to high frequency unmodeled dynamics. The outer loop was a PD controller designed using parameter space techniques. The experimental results showed the achievement of the improved dynamics with the disturbance observer in the inner loop and the successful tracking of steering commands in the outer loop. The last controller was a steering based yaw stability controller. In the design of the yaw stability controller a multi-objective design method was used to map  $D$ -stability, mixed sensitivity and phase margin bounds into the parameter space of chosen disturbance observer based steering controller filter parameters. The resulting controller design was tested using offline and hardware-in-the-loop simulations. Offline and hardware-in-the-loop simulation results showed the effectiveness of the controller design proposed in this study in tracking desired steering dynamics and in rejecting undesired yaw disturbance moments.



## REFERENCES

- [1] EU white paper, European Transport Policy for 2010, a Time to Decide, ISBN: 92-894-0341-1, 2001.
- [2] **Ackermann J., Guldner J., Sienel W., Steinhauser R.**, 1995, Linear and NonLinear Controller Design for Robust Automatic Steering, *IEEE Transactions On Control Systems Technology* Vol 3, No. 1.
- [3] **J. Ackermann, P. Blue, T. Bunte, L. Güvenç, D. Kaesbauer, M. Kordt, M. Muhler and D. Odenthal**, 2002, Robust Control: the Parameter Space Approach, Springer-Verlag.
- [4] **Ackerman**, Lecture Notes on Robust Control
- [5] **Ackermann J., Bartlett A., Kaesbauer D., Sienel W., Steinhauser R.**, 1993, Robust Control: Systems with Uncertain Physical Parameters, Springer-Verlag.
- [6] **Güvenç, L.**, Lecture Notes on Vehicle Dynamics and Control
- [7] **Rajamani R.,(2006)**, Vehicle Dynamics and Control, Mechanical Engineering Series, Springer
- [8] <http://en.wikipedia.org/wiki/>
- [9] **Genta, G.**, 1997. Motor Vehicle Dynamics: Modelling and Simulation, Singapore ; River Edge, NJ : World Scientific.
- [10] **Parmar, M., and Hung J. Y.**, 2004, A Sensorless Optimal Control System for an Automotive Electric Power Assist Steering System, *IEEE Transactions on Industrial Electronics*, Vol 51, No. 2, April 2004 .
- [11] **Çetin, E., Sinanoğlu, B., Güngör, S., Kanbolat, A., Adli, M. A.**, 2005, Compliant Control of Electric Power Assited Steering Systems, SAE Commercial Vehicle Engineering Conference
- [12] [www.dspace.de](http://www.dspace.de)
- [13] **Kim, J.H., Song, J.B.**, 2002, Control Logic for an Electric Power Steering System Using Assist Motor, *Mechatronics*, 12, 447-459
- [14] **McCann, R.**, 2000, Variable Effort Steering for Vehicle Stability Enhancement Using an Electric Power Steering System, *SAE Technical Paper Series* 2000-01-0817

- [15] **Vijayakumar, S., Chandran, R.**, 2003, Analysis of an Electric Power Assisted System using Bond Graphs,” *SAE Technical Paper Series* , 2003-01-0586.
- [16] **Chabaan, R. C., Wang, L. Y.**, 2001, Control of Electrical Power Assist Sytems: Hinf. Design, Torque Estimation and Structural Stability, Society of Automotive Engineers of Japan Inc. and Elsevier Science
- [17] **Liao, Y. G., and Du H. I.**, 2003, Modelling and Analysis of Electric Power Steering System and its Effect on Vehicle Dynamic Behaviour, *International Journal of Vehicle Autonomous Systems*, Vol 1., No.2
- [18] **Zaremba, A., Davis, R.I.**, 1995, Dynamic Analysis and Stability of a Power Assist Steering System, *Proceedings of The American Control Conference*, Seattle, Washington, June 1995, pp. 4253-4257
- [19] **Sherman, D.**, Bosch-ZF Active Steering: Mechanical and Electronic Guidance Controls Coexisting Harmoniously, <http://www.zf.com/>
- [20] <http://www.bmwworld.com/technology/afs.htm>.
- [21] **Kim, B.K., Chung, W.K.**, 2003, Advanced Disturbance Observer Design for Mechanical Positioning Systems, *IEEE Transactions on Industrial Electronics*, vol. 50, no. 6, December
- [22] **Ohnishi, K.**, 1987, A New Servo Method in Mechatronics, *Trans. Japanese Soc. Elect. Eng.*, vol. 107-D, pp. 83-86
- [23] **Umeno, T. and Hori, Y.**, (1991), Robust Speed Control of DC Servomotors Using Modern Two Degrees-of-Freedom Controller Design , *IEEE Transactions on Industrial Electronics*, vol 38, no. 5, pp. 363-368.
- [24] **Karaman, S., Öncü, S., Güvenç, L., Ersolmaz, Ş.S., Çetin, E., Kanbolat, A.**, 2006, Robust Velocity Scheduled Yaw Stability Control of a Light Commercial Vehicle, *IEEE Intelligent Vehicles Symposium*, Tokyo, 2006, June 13-15.
- [25] **Öncü, S., Karaman, S., Güvenç, L., Ersolmaz, S., Öztürk, E., Çetin, E., Sinal, M.**, 2007, Robust Yaw Stability Controller Design for a Light Commercial Vehicle Using a Hardware in the Loop Steering Test Rig, *IEEE Intelligent Vehicles Symposium*, Istanbul, 2007, June 13-15
- [26] **van Zanten, A.T., Erhardt, R. and Pfaff, G.**, 1995, VDC, The Vehicle Dynamics Control System of Bosch. SAE paper No. 950759
- [27] **L. Güvenç, J. Ackermann**, Links Between the Parameter Space and Frequency Domain Methods of Robust Control, *International Journal of Robust and Nonlinear Control*, vol. 11, 2001, pp. 1435-1453.

## **APPENDICES**

### **APPENDIX A. Technical Specifications of dSpace Systems**

## APPENDIX A.

Parameter	Symbol	Conditions / Comments	Min	Typ	Max	Units
<b>Analog Inputs</b>						
ADC Type 1 (all 16 channels)	$V_{maxADC}$	Full scale	4.84	5.00	5.16	V
	Resolution	No missing codes	12			bit
	Offset error	Errors eliminated by software compensation	0.5			LSB
	Gain error		0.5			LSB
	Offset error	$T_{CASE} = -40^{\circ}C \dots +85^{\circ}C$	-10		+10	LSB
	Gain error		-50		+50	LSB
	$Z_{inADC}$	Input impedance	150k $\Omega$ + 75k $\Omega$ /220pF			typ.
Group 4 & Group 5	$V_{maxADCG45}$	Full scale	4.7	5.0	5.3	V
	Resolution		10			bit
	Offset error	Errors eliminated by software compensation	0.5			LSB
	Gain error		0.5			LSB
	Offset error	$T_{CASE} = -40^{\circ}C \dots +85^{\circ}C$	-10		+10	LSB
	Gain error		-50		+50	LSB
	$R_{inG45}$	Input impedance	100			k $\Omega$
<b>Digital Outputs</b>						
CTM & Group 1 & Group 2 & Group 3 & Group 6 & TPU	$V_{oH}$	$I_L = 0mA$ ; $V_{DRIVE} = 5V$	3.1	4.5		V
	$V_{oL}$	$I_L = 0mA$ ; $V_{DRIVE} = 5V$		0.2	0.85	V
	$V_{oH}$	$I_L = 5mA$ ; $V_{DRIVE} = 5V$	3.1	3.4		V
	$V_{oL}$	$I_L = -5mA$ ; $V_{DRIVE} = 5V$		0.6	0.85	V
	$V_{oH}$	$I_L = 0mA$ ; $V_{DRIVE} = 12V$	10.1	11.5		V
	$V_{oL}$	$I_L = 0mA$ ; $V_{DRIVE} = 12V$		0.25	0.85	V
	$V_{oH}$	$I_L = 5mA$ ; $V_{DRIVE} = 12V$	10.1	10.4		V
	$V_{oL}$	$I_L = -5mA$ ; $V_{DRIVE} = 12V$		0.6	0.85	V
	$ I_{O_{Hmax}} $	Output current high; $T_{CASE} = -40^{\circ}C \dots +85^{\circ}C$	5	12.5		mA
	$ I_{O_{Lmax}} $	Output current low $T_{CASE} = -40^{\circ}C \dots +85^{\circ}C$	5	13		mA
<b>Analog Outputs</b>						
DAC1 ... DAC8	$V_{DAC}$	Full scale	4.44	4.50	4.56	V
	Resolution	Full monotonic	12			bit
	Offset error	Errors eliminated by software compensation	2			mV
	Gain error		0.5			LSB
	Offset error	$T_{CASE} = -40^{\circ}C \dots +85^{\circ}C$	-10		+10	LSB
	Gain error		-20		+20	LSB
	$I_{DACout}$	max. sink/ source current	-5		5	mA
	$V_{DACSAT}$	Output voltage when sinking $I_{DACout} = -5mA$ and CODE = 000H			0.3	V

Figure A.1: IO Characteristics of MicroAutobox [11]

## Technical Details

Parameter		Specification
General		<ul style="list-style-type: none"> <li>■ 6 slots for configurable, analog or digital signal conditioning modules (SC modules), (p. 17)</li> <li>■ Support of modules with different form factors (single size and double size)</li> <li>■ 2 slots for communication interface modules (e.g., USB host interface, LVDS slave interface)</li> <li>■ Unit Connection Bus to expand RapidPro Control Unit with several RapidPro Power and/or SC Units</li> <li>■ Internal temperature and voltage monitoring</li> <li>■ Remote control input to switch the unit on or off</li> <li>■ Power management, sleep and wake-up via prototyping system</li> </ul>
Microcontroller module		<ul style="list-style-type: none"> <li>■ MPC565, 56 MHz</li> <li>■ 4-MB external SRAM, 16-MB external flash</li> <li>■ On-board FPGA for additional functionality</li> <li>■ 48-channel time processing unit (TPU)</li> <li>■ 22-channel multi I/O timer (MIO5)</li> <li>■ 40-channel bit I/O</li> <li>■ 2 queued A/D converters with internal sample/hold</li> <li>■ 40 A/D converter channels (10-bit resolution, 4 <math>\mu</math>s conversion time per channel)</li> </ul>
Software support	Configuration	■ Configuration of all connected units and modules from a host PC via ConfigurationDesk (p. 7)
	Diagnostics	<ul style="list-style-type: none"> <li>■ Diagnostics handling via ConfigurationDesk (p. 7)</li> <li>■ Interactive diagnostics feedback to the model via RTI Control Unit Blockset (p. 8)</li> </ul>
	I/O Real-Time Interface	■ RTI RapidPro Control Unit Blockset (p. 8)
Electrical characteristics	Power supply	<ul style="list-style-type: none"> <li>■ +6 ... +60 V DC</li> <li>■ Load dump protection up to +100 V</li> <li>■ Voltage reverse protection up to -100 V</li> </ul>
	Enclosure	<ul style="list-style-type: none"> <li>■ Aluminum box with cooling fins (no fan)</li> <li>■ Advanced mechanical concept with special couler dips for easy mounting and module locking</li> <li>■ Enclosure designed for flexible assembly (stack or single unit)</li> </ul>
Mechanical characteristics	Physical size (with cover and base plate)	<ul style="list-style-type: none"> <li>■ l: 200 mm (7.87 in.)</li> <li>■ w: 225 mm (8.86 in.)</li> <li>■ h: 35 mm (1.38 in.)</li> </ul>
	Physical size (without cover and base plate)	<ul style="list-style-type: none"> <li>■ l: 172 mm (6.77 in.)</li> <li>■ w: 225 mm (8.86 in.)</li> <li>■ h: 25 mm (0.98 in.)</li> </ul>
Environmental characteristics	Operating temperature range	■ -40 ... +85 °C (-40 ... +185 °F)

**Figure A.2:** Technical Specifications of RapidPro SC Unit [11]

#### Technical Details

Parameter		Specification
General		<ul style="list-style-type: none"> <li>■ 6 slots for configurable power stage modules (PS modules), (p. 18)</li> <li>■ Support of modules with different form factors (single size and double size)</li> <li>■ Up to 48 power stage channels per power unit</li> <li>■ Unit Connection Bus for use with RapidPro Control Unit (p. 14)</li> <li>■ USB interface for communication with host PC</li> <li>■ SPI interface for diagnostics with MicroAutoBox</li> <li>■ Internal temperature and voltage monitoring</li> <li>■ Remote control input to switch the unit on or off</li> <li>■ Enable/disable input to switch all outputs of a unit on or off</li> <li>■ Defined "powered-off" state during initialization and booting</li> </ul>
Software support	Configuration	■ Configuration of the PS modules from a host PC via ConfigurationDesk (p. 7)
	Diagnostics	<ul style="list-style-type: none"> <li>■ Diagnostics handling via ConfigurationDesk (p. 7)</li> <li>■ Interactive diagnostics feedback to the model via RTI Control Unit Blockset (p. 8)</li> </ul>
Electrical characteristics	Power supply	<ul style="list-style-type: none"> <li>■ +6 ... +60 V DC</li> <li>■ Load dump protection up to +100 V</li> <li>■ Reverse voltage protection up to -100 V</li> </ul>
Mechanical characteristics	Enclosure	<ul style="list-style-type: none"> <li>■ Aluminum box with cooling fins (no fan)</li> <li>■ Advanced mechanical concept with special couler clips for easy mounting and module locking</li> <li>■ Enclosure designed for flexible assembly (stack or single unit)</li> </ul>
	Physical size (with cover and base plate)	<ul style="list-style-type: none"> <li>■ l: 200 mm (7.87 in.)</li> <li>■ w: 225 mm (8.86 in.)</li> <li>■ h: 35 mm (1.38 in.)</li> </ul>
	Physical size (without cover and base plate)	<ul style="list-style-type: none"> <li>■ l: 172 mm (6.77 in.)</li> <li>■ w: 225 mm (8.86 in.)</li> <li>■ h: 25 mm (0.98 in.)</li> </ul>
Environmental characteristics	Operating temperature range	■ -40 ... +85 °C (-40 ... +185 °F)

**Figure A.3:** Technical Specifications of RapidPro PU Unit [11]

## **VITA**

**Candidate's full name:** Sinan Öncü

**Place and date of birth:** Manisa,1981

**Universities and Colleges attended:** Istanbul Technical University - Electronic and Communications Engineering (2000-2005)  
Istanbul Technical University  
Mechatronics Engineering (2005- )

### **Publications:**

S. Öncü, L. Güvenç, S. Ersolmaz, S. Öztürk, N. Kılıç, M. Sinal, Steer-by-Wire Control of a Light Commercial Vehicle Using a Hardware-in-the-Loop Test Setup, *SAE Commercial Vehicle Engineering Congress* paper no: 2007-01-4198

S. Öncü, S. Karaman, L. Güvenç, S.S. Ersolmaz, E.S. Öztürk, M. Sinal , Robust Yaw Stability Controller Design for a Light Commercial Vehicle Using a Hardware in the Loop Steering Test Rig, *IEEE Intelligent Vehicle Symposium 2007*, Istanbul, Turkey, June 13-15 2007,

S. Karaman, S. Öncü, L. Güvenç, S.S. Ersolmaz, E. Çetin, A. Kanbolat, Robust velocity scheduled yaw stability control of a light commercial vehicle, *IEEE Intelligent Vehicle Symposium 2006*, Tokyo, Japan, June 13-15 2006,

L. Güvenç, Ş.S. Ersolmaz, S. Öncü, E.S. Öztürk, E. Çetin, N. Kılıç, Stability Enhancement of a Light Commercial Vehicle Using Active Steering, *SAE Conference* paper no: 2006-01-1181